

LGEST: Dynamic Spatial-Spectral Expert Routing for Hyperspectral Image Classification

Jiawen Wen^{a,b}, Suixuan Qiu^b, Zihang Luo^c, Xiaofei Yang^{c,*}, Haotian Shi^c

^aInformation Hub, The Hong Kong University of Science and Technology (Guangzhou), Guangzhou, 511453, China

^bFaculty of Geographical Science, Beijing Normal University, Beijing, 100875, China

^cSchool of Electronic and Communication Engineering, Guangzhou University, Guangzhou University, Guangzhou, 510006, China

Abstract

Deep learning methods, including Convolutional Neural Networks, Transformers and Mamba, have achieved remarkable success in hyperspectral image (HSI) classification. Nevertheless, existing methods exhibit inflexible integration of local-global representations, inadequate handling of spectral-spatial scale disparities across heterogeneous bands, and susceptibility to the Hughes phenomenon under high-dimensional sample heterogeneity. To address these challenges, we propose Local-Global Expert Spatial-Spectral Transformer (LGEST), a novel framework that synergistically combines three key innovations. The LGEST first employs a Deep Spatial-Spectral Autoencoder (DSAE) to generate compact yet discriminative embeddings through hierarchical nonlinear compression, preserving 3D neighborhood coherence while mitigating information loss in high-dimensional spaces. Secondly, a Cross-Interactive Mixed Expert Feature Pyramid (CIEM-FPN) leverages cross-attention mechanisms and residual mixture-of-experts layers to dynamically fuse multi-scale features, adaptively weighting spectral discriminability and spatial saliency through learnable gating functions. Finally, a Local-Global Expert System (LGES) processes decomposed features via sparsely activated expert pairs: convolutional sub-experts capture fine-grained textures, while transformer sub-experts model long-range contextual dependencies, with a routing controller dynamically selecting experts based on real-time feature saliency. Extensive experiments on four benchmark datasets demonstrate that LGEST consistently outperforms state-of-the-art methods.

Keywords: Hyperspectral Image Classification, Transformers, Convolution Neural Network, MoE

1. Introduction

Hyperspectral images (HSIs) capture contiguous spectral bands across the electromagnetic spectrum, forming 3D data cubes rich in spatial and spectral information. These enable fine-grained material discrimination critical for military reconnaissance [1], precision agriculture [2], and mineral exploration [3]. However, HSI classification faces inherent challenges: high dimensionality, spectral-spatial heterogeneity, and complex inter-band correlations that hinder accurate pixel-level categorization. HSI classification aims to assign each pixel in the HSI to a specific land-cover class. The HSI classification methods could be divided into two categories: Traditional methods and Deep learning-based methods. Traditional methods rely on spectral signatures while ignoring spatial context. For example, Support Vector Machine (SVM) [4, 5] separate classes via optimal hyperplanes but falter with nonlinear data distributions. K-Nearest Neighbor (KNN) [6] leverages spectral similarity metrics yet suffers from the “curse of dimensionality”. Multiple Linear Regression (MLR) [7] class probabilities linearly but fails to capture spatial dependencies. However, these methods share critical limitations: inability to jointly model spectral-spatial features, sensitivity to noise, and poor scalability to high-dimensional data.

With the rapid development of deep learning, it has been widely applied to HSI classification, showing great potential in addressing the limitations of traditional methods. Convolutional neural networks (CNNs) are particularly effective in this task due to their hierarchical structure, which inherently captures local spatial patterns and spectral correlations. 2D-CNNs treat HSIs as two-dimensional images and mainly focus on spatial feature extraction. For example, Yang *et al.* [8] leveraging 2D-CNNs extract spatial features through stacked convolutional layers. In contrast, 3D-CNN frameworks address this issue by directly processing the 3D HSI data cube, jointly extracting spectral and spatial features. For example, Chen *et al.* [9] pioneered joint spectral-spatial feature learning, and Hamida *et al.* [10] demonstrated enhanced discriminative power with deeper 3D architectures. Despite these advances, these approaches continue to face significant constraints. However, CNN-based methods also have problems. 2D-CNNs may not fully utilize the spectral information, and 3D-CNNs often suffer from high computational complexity and a large number of parameters, which can lead to overfitting, especially when the number of training samples is limited.

Transformer architectures have emerged as powerful solutions for HSI classification by leveraging self-attention mechanisms to model global dependencies. For example, Yang *et al.* [11] pioneers this approach by integrating 3D convolutions within transformer blocks to capture joint spatial-spectral relationships. However, it enforces uniform attention across spectral bands, failing to account for band-specific noise profiles. SpectralFormer [12] addresses spec-

*Corresponding author: Xiaofei Yang

E-mail addresses: jwen341@connect.hkust-gz.edu.cn (J. Wen), qiusuixuan@mail.bnu.edu.cn (S. Qiu), 1275174812@e.gzhu.edu.cn (Z. Luo), xiaofeiyang@gzhu.edu.cn (X. Yang), shihaotian@gzhu.edu.cn (H. Shi)

tral continuity through frequency-domain attention but neglects fine-grained spatial structures critical for boundary preservation. However, they also have limitations. Transformers typically require a large number of parameters and computational resources, which can be a burden for processing HSIs, especially on devices with limited computing power. They may also struggle with local feature extraction, as their self-attention mechanisms are more focused on global relationships.

Recently, Mamba-based methods have started to be explored in HSMamba classification. Mamba, a new neural network architecture, has the potential to offer advantages in terms of computational efficiency and scalability. For example, MambaHSI [13] offer efficient long-range modeling but struggle with local texture preservation and spectral-spatial feature alignment. Additionally, in the context of image classification in general, Mixture-of-Experts (MoE) models have shown promise. MoE models consist of multiple "expert" sub-models, each specialized in different aspects of the data. In HSI classification, MoE can be used to handle the diverse characteristics of HSIs, such as different spectral patterns and spatial structures. For example, Switch Transformers [14] improve model capacity via sparse activation but remain unexplored for spectral-spatial adaptive routing in HSIs.

Although CNN-based, Transformer-based, and Mamba-based approaches have advanced hyperspectral image (HSI) classification, several challenges persist. CNN-based methods exhibit limitations: 2D CNNs insufficiently exploit spectral information, while 3D CNNs incur high computational complexity and a heightened risk of overfitting. Transformer-based approaches require considerable computational resources and tend to extract local features less effectively. Although Mamba-based methods demonstrate potential, they remain in the early exploratory phase and require further refinement to fully leverage the unique properties of HSIs. Furthermore, MoE-based approaches call for improved integration strategies to ensure cohesive collaboration among diverse experts and to effectively manage the complexity and high dimensionality of HSI data.

To address these challenges, we introduce LGEST, a novel method that comprehensively overcomes the limitations of existing approaches. Previous methods have either concentrated solely on local or global features or lacked an effective mechanism for integrating diverse types of information. In contrast, LGEST utilizes a local-global expert mechanism, wherein the local experts are designed to capture intricate spectral-spatial features, and the global experts employ a transformer-like architecture that excels at modeling long-range dependencies and capturing broad contextual information. By integrating both local and global experts, LGEST effectively harnesses the full spectrum of information present in hyperspectral images (HSIs). Moreover, inspired by the success of mixture-of-experts (MoE) frameworks in managing heterogeneous data characteristics, LGEST incorporates an MoE-inspired structure within its local and global components. This design enables individual experts to specialize in various aspects of HSI data, such as distinct spectral bands or spatial regions. For example, some local experts may focus on edge-related features within specific spectral ranges, while others capture texture variations across different spatial scales. Similarly, the global experts may specialize in modeling diverse global relationships, including overarch-

ing spectral trends or extensive spatial patterns. This innovative integration of local-global information, coupled with an MoE-inspired architecture, is anticipated to significantly enhance the classification performance of HSIs.

In summary, the contributions of our proposed LGEST method are as follows:

1. We propose LGEST, a novel hybrid framework for hyperspectral image classification that dynamically integrates local-global feature via sparsely activated experts, being the first to achieve such integration.
2. We introduce a **Deep Spatial-Spectral Autoencoder (DSAE)** to learn compact and discriminative 3D spectral-spatial features through hierarchical nonlinear compression while preserving 3D neighborhood coherence.
3. We develop a **Cross-Interactive Mixed Expert Feature Pyramid (CIEM-FPN)**, the novel MoE-enhanced feature pyramid, which uses cross-attention for adaptive spectral-spatial weighting to capture multi-scale features.
4. We design a performance-oriented **Local-Global Expert System (LGES)** that resolves spectral-spatial misalignment via Confidence-aware routing to achieve 3D spectral-spatial features.
5. We conduct extensive experiments on four hyperspectral datasets, demonstrating the superiority of LGEST over existing methods.

2. Related Work

2.1. CNN-based Hyperspectral Image Classification Methods

Convolutional neural networks (CNNs) have been widely applied to HSI classification due to their superior local perception capabilities and effectiveness in extracting spatial context information [15]. Many researchers have designed 2D CNNs for this task, such as the one proposed by Yang *et al.* [8] which consists of three 2D convolutional layers and a fully connected layer. However, these 2D CNNs extract features by separating spatial and spectral dimensions. To address this, Chen *et al.* proposed a 3D CNN architecture using 3D convolution to extract spatial-spectral features [9]. Some other methods introduce 3D convolution to jointly process spectral and spatial information, such as the work by Hamida *et al.* [10] and the Synergistic Convolutional Neural Network (SyCNN) designed by Yang *et al.* [16].

While 3D CNNs jointly model spatial-spectral features, their fixed receptive fields struggle to balance local texture preservation (e.g., crop boundaries) and global context capture (e.g., large-scale mineral distributions). Hybrid designs like HybridSN [17] combine 3D and 2D convolutions but use rigid cascades, causing spectral over-smoothing in noisy bands. Recent work by Xi *et al.* [18] addresses class imbalance but retains static multi-scale fusion, limiting adaptability to heterogeneous scenes. These limitations underscore the need for dynamic architectures that co-optimize local and global feature hierarchies — a gap addressed by our LGES.

2.2. Transformers-based Hyperspectral Image Classification Methods

Recently, transformer networks have gained prominence in natural language processing and have since been applied to image classification tasks. Following the pioneering work of Dosovitskiy *et al.* [19], several studies have addressed the issue of attention collapse in deep Vision Transformer (ViT) models, where feature maps tend to be identical in the top layers. To mitigate this, Zhou *et al.* [20] proposed DeepViT, which introduced a re-attention mechanism using a learnable matrix to enhance attention map diversity. Yang *et al.* [21] introduced a new Quaternion Transformer Network (QTN) designed to capture self-adaptive and long-range correlations in HSI classification. Conventional transformers often process 2D images as 1D sequences, limiting their ability to extract joint spatial-spectral features. To address this, researchers have incorporated convolution operations into transformer networks [22, 23, 24, 11, 25, 26, 27, 28, 29, 30]. For example, Yang *et al.* introduced spectral-adaptive 3D convolutions within a transformer, creating the hyperspectral image transformer (HiT) network [11] to capture local spatial-spectral features.

Vision transformers like HiT [11] integrate 3D convolutions for local spectral-spatial modeling but enforce uniform attention across all bands, neglecting band-specific noise profiles. ISSFormer [26] improves feature interaction but uses fixed fusion rules, failing to dynamically prioritize spatial or spectral cues (e.g., suppressing noisy urban bands while enhancing mineral-sensitive ones). Recent lightweight transformers [28] optimize efficiency but sacrifice spectral discriminability through aggressive token pruning. These works highlight a critical need for dynamic resource allocation—a capability uniquely enabled by LGEST’s Confidence-aware expert routing.

2.3. Mamba-based Hyperspectral Image Classification Methods

Mamba-based models have emerged as efficient alternatives for sequence modeling, with applications in HSI classification [31, 32, 33, 34, 35]. For example, MambaHSI [13] employs the Mamba architecture to capture long-range spatial-spectral dependencies, while 3DSS-Mamba [31] introduces spectral space tag generation (SSTG) with 3D selective scanning. MambaLG [36] adopts a dual-branch structure to extract local and global background information. These studies primarily focus on aligning raw HSI inputs with the Mamba architecture. However, constructing state space models (SSMs) in this manner may reduce both local spatial invariance and computational efficiency. To address this, ConvMamba [37] integrates convolution for feature and domain fusion, IGroupSS-Mamba [38] employs Interval Group Space-Spectral Blocks (IGSSB) for contextual representation, and GraphMamba [39] incorporates HyperMamba and SpatialGCN modules for parallel and adaptive processing. Despite their advantages in handling long-range contexts, Mamba-based methods face challenges in preserving local texture details and aligning spectral-spatial features, which are critical for accurate pixel-level classification in complex HSI scenes. This highlights the need for hybrid approaches that combine the efficiency of Mamba with mechanisms to enhance local feature preservation and multi-modal alignment.

3. Proposed Approach

3.1. Overview of LGEST

Hyperspectral image data is a three-dimensional data structure that contains both spatial and spectral information. This information can be represented by a three-dimensional tensor $H \in \mathbb{R}^{W \times H \times C}$, where W and H represent spatial information and carry the HSI dataset’s spatial dimensions, while C represents spectral information. Numerous studies have demonstrated that integrating spatial and spectral information can improve HSI classification performance. Therefore, our model incorporates both local-global and spatial-spectral information to enhance hyperspectral image classification. We achieve this through the design of a cross-interactive mixed expert feature pyramid, which explores long-term spatial-spectral relationships between different image elements and the global spectral properties of individual image elements.

As shown in Fig. 1 and Algorithm 1, our model consists of three main components: the deep spatial-spectral auto-encoder (DSAE), the cross-interactive mixed expert feature pyramid (CIEM-FPN), and the local-global expert system (LGES). Multiple mixture of experts layers are incorporated into CIEM-FPN and the LGES. Critically, we employ a hierarchical decoupling strategy where these two expert systems address distinct challenges: physical heterogeneity in the feature space and semantic ambiguity in the decision space.

Given an input $\{X, y\}$, a hyperspectral image paired with category-labeled data, we first pass X through a DSAE to extract richer local spatial information from the HSI data and obtain more compact and representative features from the high-dimensional input. The encoder generates local features F via three convolutions, which are then fed into our encoder-decoder structure to produce \hat{F} . \hat{F} is then fed into the CIEM-FPN, which has a parallel and downsampling branch to extract features from the HSI data. Functioning in the feature space, CIEM-FPN employs "Feature Alignment Experts" within the cross-interactive mixed expert module (CIEM). These experts focus on mitigating physical heterogeneity by aligning feature distributions across different scales and modalities (Spectral vs. Spatial), thereby resolving feature misalignment. The CIEM enables softer interactions between diverse features, producing the output feature P .

F and P represent local and global information. Finally, the Local-Global Expert System (LGES) transitions the processing framework into the semantic decision space. Diverging from the feature alignment objective of the preceding stage, LGES deploys 'Semantic Decision Experts' to dynamically modulate sub-expert activation. This mechanism is specifically engineered to mitigate semantic ambiguity (e.g., inter-class confusion) by adaptively arbitrating the distinct contributions of high-frequency details (e.g., fine-grained textures) and low-frequency contexts (e.g., broad spatial coverage) toward the final classification inference. The outputs P_i and P_k of the LGES are employed to compute the loss and predict the class probabilities based on the maximum score. The training loss is a weighted combination of the

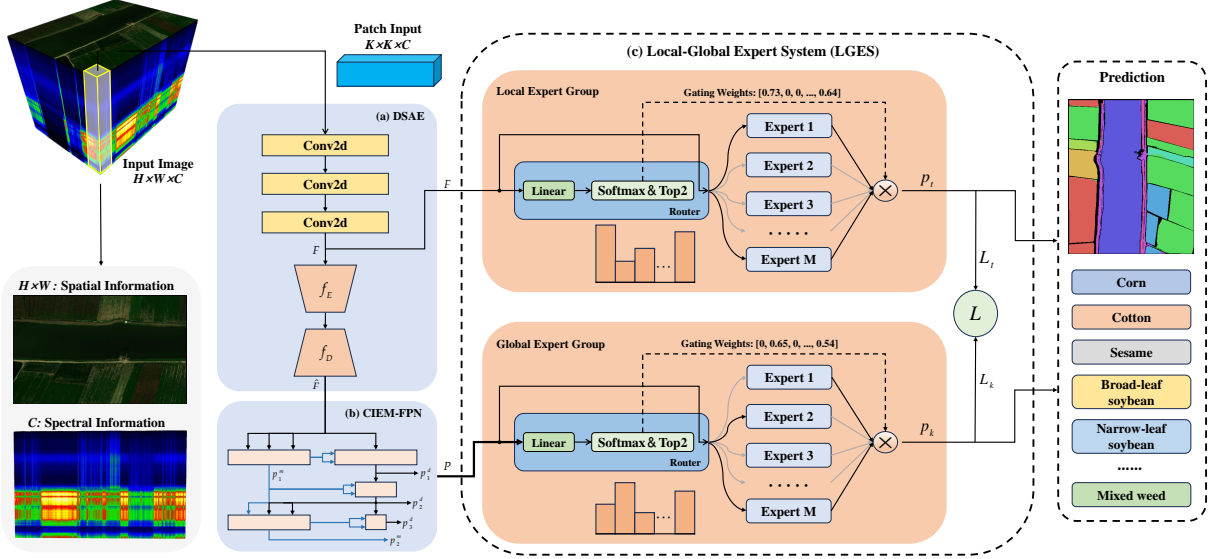


Fig. 1. The architecture of proposed LGEST. The network processes input data with a deep spatial-spectral auto-encoder (DSAE), which serves as a local feature extractor. It then uses a cross-interactive mixed expert feature pyramid to fuse features across different scales via parallel and downsampling branches, enhancing interactions through the Cross-Interactive mixed Expert Feature Pyramid (CIEM-FPN). This is followed by the local-global expert system (LGES), divided into two expert groups handling local and global information. The router selects the activated expert from sub-experts within each group, which are linear layers.

Algorithm 1 Forward Pass of LGEST (Dynamic Spatial-Spectral Expert Routing)

Require: Hyperspectral image patch $X \in \mathbb{R}^{W \times H \times C}$, Ground truth label y

Ensure: Local predictions P_l , Global predictions P_k , Total Loss L

// Phase 1: Local Feature Extraction via Deep Spatial-Spectral Auto-Encoder (DSAE)

- 1: $F \leftarrow f_{conv}(X)$ \triangleright Extract local spatial features via Conv2d
- 2: $K \leftarrow f_E(F)$ \triangleright Encoder: hierarchical nonlinear compression
- 3: $\hat{F} \leftarrow f_D(K)$ \triangleright Decoder: reconstruct compact features

// Phase 2: Global Context Modeling via Cross-Interactive Mixed Expert Feature Pyramid (CIEM-FPN)

- 4: Initialize feature lists for multi-scale fusion
- 5: **for** level $i = 1$ to num_fpn_level **do**
- 6: $F_c \leftarrow CA(Q_i, K_i, V_i)$ \triangleright Dynamically adjust fusion weights
- 7: $P_i \leftarrow F_{RMoE}(F_c + Q_i)$ \triangleright Mitigate physical heterogeneity
- 8: **end for**

- 9: $P \leftarrow Concat(P_1, P_2, \dots, P_{num_fpn_level})$ \triangleright Aggregate multi-scale features

// Phase 3: Semantic Decision via Local-Global Expert System (LGES)

// 3.1 Local Expert Group (Addressing local texture confusion)

- 10: $S_{local} \leftarrow \text{Softmax}(W_{g_local}^T F + b_{g_local})$
- 11: $\mathcal{T}_{local} \leftarrow \text{Top2}(S_{local})$ \triangleright Select indices of the top-2 experts
- 12: $S'_{local} \leftarrow S_{local} \cdot \text{Mask}(\mathcal{T}_{local})$ \triangleright Sparse activation masking
- 13: $P_l \leftarrow \sum_{j \in \mathcal{T}_{local}} S'_{local}[j] \cdot \text{Expert}_j^{local}(F)$

// 3.2 Global Expert Group (Addressing global spectral variability)

- 14: $S_{global} \leftarrow \text{Softmax}(W_{g_global}^T P + b_{g_global})$
- 15: $\mathcal{T}_{global} \leftarrow \text{Top2}(S_{global})$ \triangleright Select indices of the top-2 experts
- 16: $S'_{global} \leftarrow S_{global} \cdot \text{Mask}(\mathcal{T}_{global})$ \triangleright Sparse activation masking
- 17: $P_k \leftarrow \sum_{j \in \mathcal{T}_{global}} S'_{global}[j] \cdot \text{Expert}_j^{global}(P)$

// Phase 4: Optimization

- 18: $Loss(P_l) \leftarrow \text{CrossEntropy}(P_l, y)$
- 19: $Loss(P_k) \leftarrow \text{CrossEntropy}(P_k, y)$
- 20: $L \leftarrow \lambda \cdot Loss(P_l) + \beta \cdot Loss(P_k)$ \triangleright Compute final weighted loss
- 21: **return** P_l, P_k, L

cross-entropy losses for both.

$$Loss(\hat{x}, y) = - \sum_{i=1}^n y \log(\hat{x}) \quad (1)$$

$$L = \lambda Loss(P_l) + \beta Loss(P_k). \quad (2)$$

Where y represents the true label, while \hat{x} signifies the probability distribution associated with the predicted class. The values of two hyperparameters, λ and β , are utilized to maintain a balanced relationship between the different types of losses. Unless specified otherwise, the default settings for these hyperparameters are $\lambda = 1$ and $\beta = 0.5$.

3.2. Deep Spatial-Spectral Auto-Encoder (DSAE)

Hyperspectral images have rich spectral information, but their high dimensionality increases computational complexity and overfitting risk. As network layers grow, local spatial information (e.g., edges, texture) in HSI is lost, though it's crucial for pixel-by-pixel classification. To address these challenges, a dual-stream output architecture is employed in the DSAE module, where convolutional layers are first used to capture the raw spatial information and improve the local spatial dependency. The deep autoencoder compresses input data into a low-dimensional representation through successive nonlinear layers and then reconstructs it into the original high-dimensional space. This encoding-decoding process yields compact spatial-spectral features that retain essential information, thereby facilitating more effective extraction of global patterns.

Specifically, the DSAE module consists of three convolutional layers, a convolutional encoder f_E , and a deconvolutional decoder f_D . Given an input feature X , the feature map F is first generated by passing X through the three convolutional layers. This output feature F is then fed into the encoder f_E and the decoder f_D . Both the encoder and decoder consist of a convolutional layer, a BatchNorm layer, and a LeakyReLU nonlinear activation layer.

The convolutional encoder progressively reduces the dimensionality of the feature map. Initially, the feature map F is passed through the first convolutional layer, which generates a set of feature maps with C_1 output channels:

$$F_1 = \text{Conv}(X, C_1) \quad (3)$$

Subsequent layers halve the number of output channels, progressively compressing the feature representation. After L convolutional encoders, the output feature map K has $\frac{C_0}{2^L}$ channels, where C_0 is the initial number of channels in X . The final output of the convolutional encoder is given by:

$$K = f_E(F_L) = \text{Conv}(F_L, C_L) \quad (4)$$

where $C_L = \frac{C_0}{2^L}$ is the number of channels after L layers.

The de-convolutional decoder reconstructs the original feature map by progressively increasing the dimensionality of K . Each layer in the decoder doubles the number of output channels compared to the previous layer. After L de-convolutional decoders, the output feature map \hat{F} retains the same dimensionality as F . The reconstruction process is as follows:

$$\hat{F} = f_D(K_L) = \text{DeConv}(K_L, C_L, C_0) \quad (5)$$

where C_0 is the original number of channels in F and $C_L = \frac{C_0}{2^L}$ is the number of channels at the L -th layer.

The overall DSAE module can be described by the following set of equations:

$$\begin{aligned} F &= F_{\text{conv}}(X), \\ K &= f_E(F), \\ \hat{F} &= f_D(K). \end{aligned} \quad (6)$$

Where X is first transformed by the convolutional layers into F , then compressed into a low-dimensional feature K by the encoder f_E , and finally reconstructed to \hat{F} by the decoder f_D .

3.3. Cross-Interactive Mixed Expert Feature Pyramid

The FPN [40] has proven to be effective in both regression and prediction tasks in computer vision. However, its fusion process consists of basic up-sampling and down-sampling of features followed by addition, which often introduces noise and causes significant aliasing effects. Inspired by FPN, we introduce the CIEM-FPN, a parallel multiscale fusion module based on the cross-interactive mixed expert module (CIEM), to mitigate the noise generated by feature fusion at different scales and reveal deeper global relationships between spectral and spatial information across features. The CIEM-FPN fuses feature at different scales simultaneously through parallel and downsampling branches and enhances their interactions through a cross-attentional mechanism (Fig. 2(a)). The cross-attention mechanism dynamically adjusts the fusion weights of features by calculating the correlation between the Query (Q), Key (K), and Value (V) components. This approach enables the model to emphasize relevant features while disregarding irrelevant or noisy information during the fusion process, resulting in finer feature fusion[41]. Compared to basic addition operations, the cross-attention mechanism offers a more flexible and precise method for feature interaction.

The CIEM-FPN comprises a basic unit, the CIEM module (Fig. 2 (b)), which includes Layer Normalization (LN) [42], Cross-Attention [43], and the RMoE layer. Fig. 2(a) shows the Q, K, V inputs of each CIEM module. For input features Q, K , and V , LN is first applied, followed by transformation into potential space expressions via multiplication with learnable parameter matrices, resulting in F_q, F_k , and F_v .

$$\begin{cases} F_q = W_q(\text{LN}(Q)), \\ F_k = W_k(\text{LN}(K)), \\ F_v = W_v(\text{LN}(V)). \end{cases} \quad (7)$$

Where Q, K , and V represent three inputs, while W_q, W_k , and W_v represent three learnable parameter matrices. The generated F_q, F_k , and F_v are produced by the cross-attention mechanism. As depicted in Fig. 3(d), the computational expression of this mechanism is given by:

$$CA(Q, K, V) = \text{Softmax}\left(\frac{F_q F_k^T}{\sqrt{C}}\right) F_v. \quad (8)$$

Where F_q, F_k , and F_v are the input tokens, and $\frac{1}{\sqrt{c}}$ is the scaling factor. The dot product of F_q and F_k has an expectation of 0 and a variance of 1 when this scaling factor is used. Additionally, it prevents the softmax values from becoming overly large, thereby ensuring that the partial derivatives do not approach 0. When Q, K, V come from the same domain, cross-attention is self-attention.

We then add the generated cross-attention feature F_c to the input Q to create a more robust information representation. This representation is then fed into the proposed residual mixture of experts layer (RMoe Layer).

The architecture of the RMoE Layer, as depicted in Fig. 2 (c), is composed of a residual branch [14] and a main branch. The main branch involves the selection of two experts by a sparse gating function for computation, with their outputs modulated by the weights from the sparse gating function. The outputs of the two experts are combined to generate the main branch's output, which is then added to the residual branch to obtain the final output.

For an input x , the expression for the RMoE Layer is given below:

$$\begin{cases} G(x) = \text{Top2}(\text{Softmax}(x \cdot W_g)), \\ E_i(x) = x \cdot W_{e(i)}, \\ y(x) = \sum_{i=1}^n G(x) E_i(x), \\ F_{\text{RMoe}}(x) = y(x) + x. \end{cases} \quad (9)$$

Where $G(x)$ and $E_i(x)$ represent the gating and expert functions, respectively, and W_g and $W_{e(i)}$ are the learnable weight matrices. The primary role of the gating function is to compute the probability distribution across different experts and to select the two experts with the highest probabilities for activation. It is responsible for determining which tokens are to be allocated to which expert. The gating mechanism dynamically activates specific sub-experts based on the class of data input into the residual mixture of expert (RMoe) Layer, increasing the model's sparsity.

In the CIEM module, we replace the traditional transformer's FFN layer with the RMoE layer, which enables the model to select different experts (submodels) for processing various types of input. Consequently, the model can

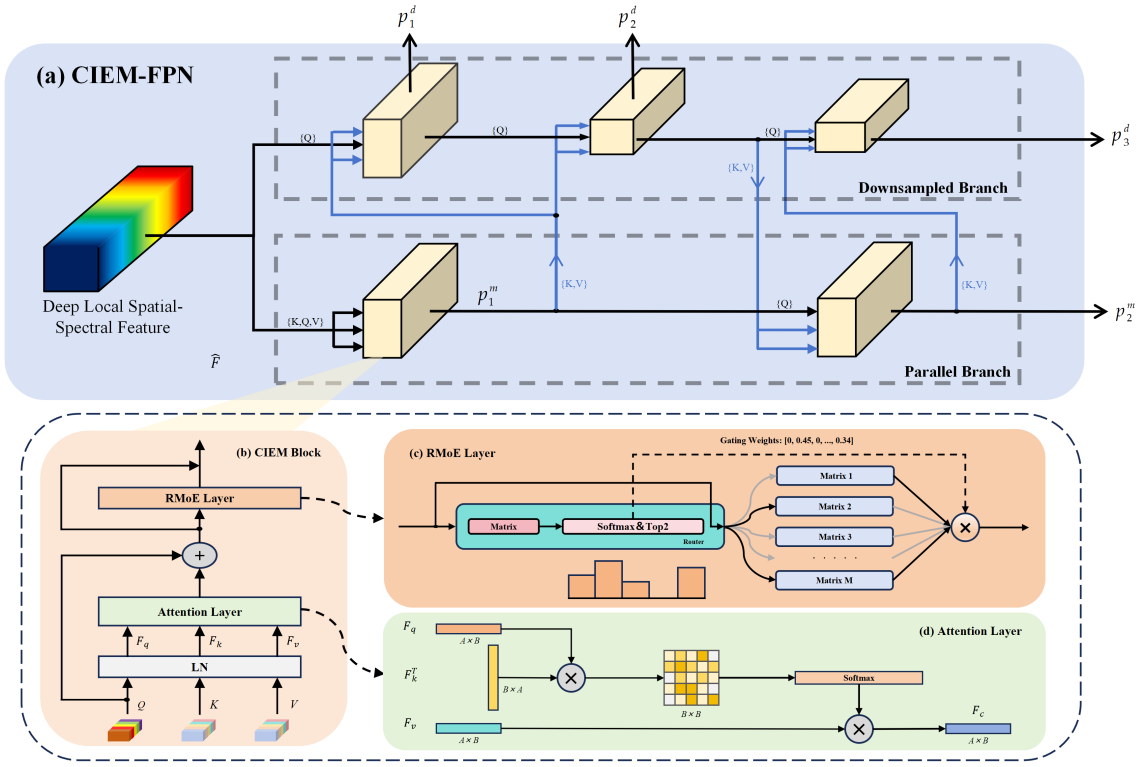


Fig. 2. The structure of the cross-interactive mixed expert feature pyramid (CIEM-FPN). (a) shows the overall framework of CIEM-FPN, which incorporates a novel cross-interactive mixed expert module (CIEM) that enhances model comprehension and generation by creating associations between different input sequences. (b) presents the detailed structure of the CIEM module. To enable cross-interactive functionality, these inputs can originate from both the parallel structure and the upper output. (c) illustrates the RMoE layer, in which the experts are learnable matrices. (d) illustrates the cross-attention mechanism employed in CIEM.

adaptively adjust its strategy for different types of input data and enhance its ability to process various spectral features. Through residual connections, the model retains the original information of the inputs when faced with unreliable expert outputs, thereby enhancing the robustness of the overall model. In summary, for the inputs Q , K , and V , the expression for the CIEM module is given by:

$$F_{CIEM} = F_{RMoE}(CA(F_q(Q), F_k(K), F_v(V)) + Q) \quad (10)$$

Where Q , K , and V denote the three inputs, F_q , F_k , and F_v represent the potential space representations of the inputs, and F_{RMoE} indicates the RMoE Layer. We construct the primary framework of the cross-interactive mixed expert feature pyramid (CIEM-FPN) based on the CIEM module. As shown in Fig.2 (a), we denote P_i^m as the output of the parallel branch (scale-invariant branch) and P_i^d as the output of the downsampled branch, where i represents the i -th layer of the branches ($i \geq 1$). We use a step size of 2 for downsampling, and for CIEM-FPN inputs $\hat{F} \in \mathbb{R}^{D \times C}$, then $P_1^m \in \mathbb{R}^{D \times C}$ and $P_1^d \in \mathbb{R}^{D \times \frac{C}{2}}$. The complete CIEM-FPN expression is as follows:

$$\begin{cases} P_i^m = F_{CIEM}(\hat{F}, \hat{F}, \hat{F}), & i = 1 \\ P_i^d = F_{CIEM}(\hat{F}, P_1^m, P_1^m), & i = 1 \\ P_i^m = F_{CIEM}(P_{i-1}^m, P_{i-1}^d, P_{i-1}^d), & i > 1 \\ P_i^d = F_{CIEM}(P_{i-1}^d, P_{i-1}^m, P_{i-1}^m), & i > 1. \end{cases} \quad (11)$$

Where P_i^m represents the output of the parallel branch (scale-invariant branch), P_i^d represents the output of the downsampled branch, i represents the i -th layer of the branch ($i \geq 1$),

and F_{CIEM} is the CIEM module. Accordingly, we can simplify the expression of CIEM-FPN as:

$$\begin{aligned} F_{CIEM-FPN}(\hat{F}) &= \{P_{L/2}^m, P_1^d, P_2^d, P_3^d, \dots, P_L^d\} \\ &= \{p_0, p_1, p_2, p_3, \dots, p_L\}. \end{aligned} \quad (12)$$

Where L indicates that there are L layers in the pyramid. To maintain a linear gradient of the output features throughout the pyramid, we use the output of the last layer of the parallel branch P_{2i-1}^m as the input to the first layer of CIEM-FPN. We concatenate all the feature vectors to obtain the final output vector P .

$$P = \text{Concat}(F_{CIEM-FPN}(\hat{F})). \quad (13)$$

Where \hat{F} is the feature input to CIEM-FPN and P is the final output of CIEM-FPN, P incorporates enhanced multiscale global features from each layer of the pyramid.

3.4. Local-Global Expert System (LGES)

Although CIEM-FPN successfully constructs a fused spatial-spectral representation by aligning heterogeneous features, mapping these high-dimensional embeddings directly to land-cover classes remains challenging due to the 'Same Spectrum Different Object' phenomenon. Distinct from the feature-level fusion in CIEM-FPN, the LGES is designed as a decision-level refinement module. While CIEM-FPN focuses on mitigating physical discrepancies (e.g., scale and noise), LGES focuses on resolving semantic ambiguities. By decoupling the classification head into local-specific and global-specific pathways, LGES ensures that the final inference is robust against both local texture confusion and

global spectral variability. This hierarchical expert design allows the model to separate feature alignment from semantic decision-making.

The Local-Global Expert System (LGES) is employed to independently process the local information provided by DSAE and the global information extracted by CIEM-FPN. Specifically, the LGES consists of two expert groups: the local expert group and the global expert group, both of which share the same structure.

As shown in Fig. 1 (c), the system consists of two expert groups processing the preliminary local feature F and the extended multiscale global interactive feature P . The structure of the two expert groups closely resembles that of the RMoE layer in CIEM, with the following distinctions: 1) In LGES, both the expert and gating mechanisms consist directly of the linear layer, and the output of the expert group, $P \in \mathbb{R}^{N \times n_{class}}$, is used directly for classification. 2) The expert group in LGES omits the residual linkage and outputs the expert's decision results directly.

The expert group is designed to dynamically aggregate outputs from multiple expert networks, allowing for adaptive computation based on the input. Let the input feature vector be $\mathbf{x} \in \mathbb{R}^d$, where d is the feature dimension. The layer consists of M expert networks, each represented as a linear transformation:

$$f_i(\mathbf{x}) = \mathbf{W}_i^T \mathbf{x} + \mathbf{b}_i, \quad i = 1, 2, \dots, M, \quad (14)$$

where $\mathbf{W}_i \in \mathbb{R}^{d \times d_{out}}$ and $\mathbf{b}_i \in \mathbb{R}^{d_{out}}$, with d_{out} being the output dimension. A gating mechanism computes the softmax-normalized weights for the experts:

$$\mathbf{s} = \text{softmax}(\mathbf{W}_g^T \mathbf{x} + \mathbf{b}_g), \quad (15)$$

where $\mathbf{W}_g \in \mathbb{R}^{d \times M}$ and $\mathbf{b}_g \in \mathbb{R}^M$. Instead of using fixed routing, we employ a content-adaptive gating mechanism. The Top-2 softmax selection naturally filters out low-confidence experts, allowing the model to focus on the most relevant feature subspaces. To reduce computational overhead, only the top-2 experts with the highest weights are selected. Let $\mathcal{T}_2 \subset \{1, 2, \dots, M\}$ denote the indices of the top-2 experts. A mask $\mathbf{m} \in \mathbb{R}^M$ is applied such that:

$$\mathbf{m}[i] = \begin{cases} 1, & \text{if } i \in \mathcal{T}_2, \\ 0, & \text{otherwise.} \end{cases} \quad (16)$$

The weights for the top-2 experts are then refined as $\mathbf{s}' = \mathbf{s} \odot \mathbf{m}$, where \odot represents element-wise multiplication. The outputs of all experts are stacked into a tensor $\mathbf{E} \in \mathbb{R}^{N \times M \times d_{out}}$, where N is the batch size, and the final output is computed as:

$$\mathbf{m}[i] = \left\{ \mathbf{y} = \mathbf{s}'^T \mathbf{E}. \right. \quad (17)$$

If the number of experts is less than 2, defined ($M = 0, 1$), the layer defaults to a single linear transformation $f_0(\mathbf{x})$. Formally, the output of the expert group can be expressed as:

$$f_{expertgroup} = \begin{cases} f_0(\mathbf{x}), & \text{if } M = 0, 1 \\ \mathbf{s}'^T \mathbf{E}, & \text{if } M > 1. \end{cases} \quad (18)$$

This design enables the expert group to adaptively utilize selected experts for efficient and flexible computation. The

complete expression for the local-global expert system is as follows:

$$\begin{cases} P_l = f_{expertgroup}(F), \\ P_k = f_{expertgroup}(P). \end{cases} \quad (19)$$

Where $f_{expertgroup}$ denotes the expert group, F is the initial localized feature, and P is CIEM-FPN output. Each expert is trained on distinct data, allowing the model to integrate expert advantages for improved classification accuracy. This approach is particularly effective for high-dimensional, high-complexity hyperspectral data. Finally, P_l and P_k are directly employed for classification and loss calculation.

4. Experiments

In this section, we evaluate the proposed LGEST on four publicly available HSI datasets: Indian Pines, Kennedy Space Center (KSC), Houston2013 and WHU-Hi-LongKou. To fully compare the effectiveness of our model, we compare LGEST with 13 other advanced HSI image classification methods. These include traditional HSI classification methods (e.g., SVM [4]), CNNs-based HSI classification methods (e.g., 2D CNN [8], 3D CNN [10], SYCNN [16], HybridSN [17]), and transformer-based HSI classification methods (e.g., ViT [19], DeepViT [20], Cross ViT [41], CaiT [44], HiT [11], SSFTT [25], Morphformer [45], SS-TMNet[22], GSC-ViT [23]). The evaluation metrics are the Overall Accuracy (OA), Average Accuracy (AA), and Kappa coefficient (κ).

4.1. Datasets and experimental settings

To evaluate the performance of LGEST, we selected four representative publicly available benchmark datasets: Indian Pines, Kennedy Space Center, Houston2013 and WHU-Hi-LongKou. Their detailed descriptions are given below:

Indian Pines Dataset: The Indian Pines dataset, collected in 1992 by the AVIRIS sensor in northwestern Indiana, contains 145×145 pixels with 200 usable spectral bands and provides 10,249 labeled samples across 16 land-cover classes at 20 m resolution.

Kennedy Space Center (KSC): The KSC dataset, collected in 1996 by NASA's AVIRIS sensor over the Kennedy Space Center, contains 512×614 pixels with 176 high-quality bands spanning visible to near-infrared wavelengths. It provides 13 land-cover classes, including wetlands, forests, and agriculture, at 18 m resolution.

Houston2013: The Houston2013 dataset, acquired in 2012 by the ITRES CASI-1500 sensor in Houston, contains 349×1905 pixels with 144 bands from visible to near-infrared and 15 land-cover classes, including trees, soil, and roads. It is widely used as a benchmark for multi-source fusion, classification, and urban planning studies.

WHU-Hi-LongKou: The WHU-Hi-LongKou dataset, collected in 2018 in Longkou Town, China, using a UAV-mounted Headwall Nano-Hyperspec sensor at 500 m altitude, contains 550×400 pixels with 270 bands (400–1000 nm) at 0.463 m spatial resolution.

Metrics: To evaluate model performance, we use Overall Accuracy (OA), Average Accuracy (AA), and Kappa Coefficient (κ), common metrics in HSI image classification.

Implementation details: All models are implemented on Ubuntu 20.04.5 with an AMD EPYC 7542 CPU and an

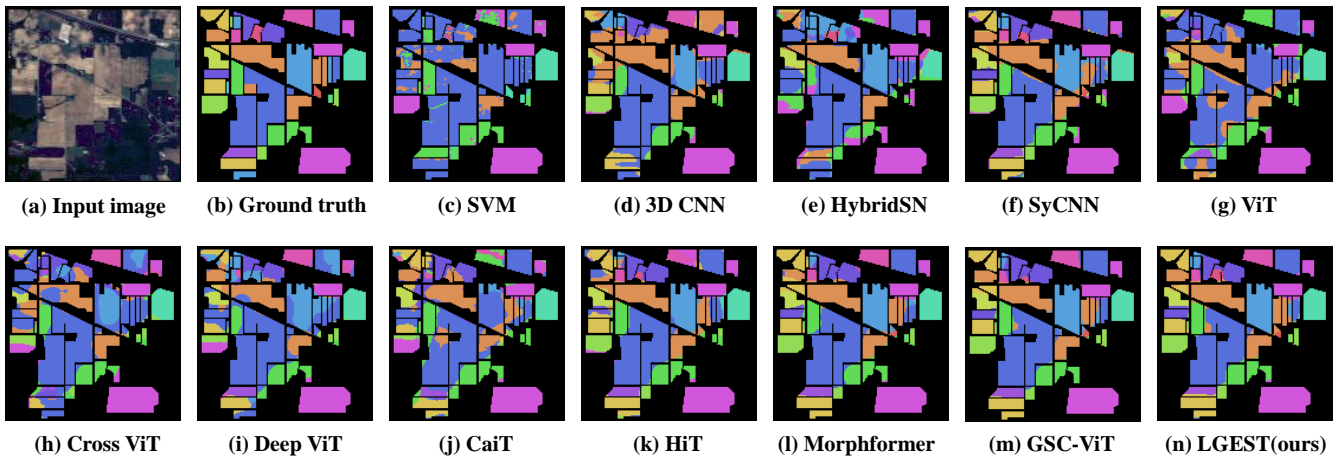


Fig. 3. Classification map of different methods on the IndianPines dataset (with 10% training samples).

NVIDIA RTX 4090 GPU using PyTorch 1.12.1. Training uses the Adam optimizer with a learning rate of $1e-3$, default settings, a batch size of 100, and 100 epochs. Each experiment is repeated 10 times. To evaluate LGEST under limited labeled data, 10% of samples are used for training on IP, KSC, and Houston2013, while only 0.1% are used for the WHU-Hi-LongKou dataset due to its relatively simple spatial structure, highlighting robustness in extremely low-label settings.

4.2. Analysis of Comparative Experiments with State-of-the-Art Models

4.2.1. Analysis of evaluation metrics results

This section will present a detailed analysis of the classification performance of the proposed LGEST in comparison to other HSI image classification methods. The results of the experiment are presented in Tables 1, 2, 3, and 4, wherein the bolded evaluation metrics represent the optimal performance.

LGEST achieved superior performance across four datasets. On IndianPines, it improved AA to $80.72 \pm 3.00\%$ (+5.38%) and uniquely classified class 9 with 12.22% accuracy. On KSC, it reached $92.59 \pm 1.44\%$ OA, outperforming convolutional methods by 7.98%, suggesting their limited use of global information. On Houston2013, LGEST improved AA by 9.64% to $95.88 \pm 0.40\%$, aided by pyramidal interactions and rich local features, with gains up to 12.91%. On WHU-Hi-LongKou, although slightly lower in OA than the second-best model, it improved AA by 3.24%. Overall, LGEST excelled by combining DSAE for local features, CIEM-FPN for global spatial-spectral interactions, and a local-global expert system for specialized processing.

4.2.2. Analysis of visualization results

To further illustrate the effectiveness of our method, Figs. 3, 4, 5 and 6 present the visualization results for all classification methods. The figures illustrate that the classification maps produced by other methods exhibit more noise and greater confusion at the boundaries between different categories, whereas the classification maps generated by our proposed LGEST method are smoother and demonstrate more accurate classification results overall.

As shown in Fig. 3, SVM produces the poorest results with frequent misclassifications. Convolution-based

methods, limited to local features, misclassify boundary regions, while transformers introduce noise and struggle with classes of small coverage due to missing local details. Transformer-convolution hybrids improve accuracy but still fail on small classes. In contrast, LGEST produces refined maps that align closely with the ground truth.

4.2.3. Analysis of t-SNE results

To more effectively demonstrate the performance of each classifier, we selected five of the most representative classification methods for comparison with the proposed LGEST using t-distributed stochastic neighbor embedding (t-SNE). As shown in Fig. 7, on the IndianPines dataset, our proposed method exhibits a smaller intra-class distance and a larger inter-class distance compared to other models, which suffer from higher intra-class confusion. In particular, the 3D CNN and ViT models yielded the poorest clustering results. Conversely, the SyCNN and HiT models demonstrated enhanced classification performance, although they still exhibited notable confusion. Morphformer exhibits clustering results comparable to those of the LGEST, yet displays a greater dispersion of scattered points and more considerable inter-class distances. In general, the results demonstrate that LGEST exhibits the most effective clustering and that the efficacy of clustering is positively correlated with classification performance.

4.3. Complexity Analysis

This section evaluates the computational efficiency of LGEST compared to representative methods using Floating Point Operations (FLOPs), number of parameters (Params), and Overall Accuracy (OA), as summarized in Table 5.

Superior Efficiency over 3D CNNs: Traditional 3D deep learning methods often suffer from high computational costs. As shown in Table 5, compared to the representative spatial-spectral model SyCNN, LGEST reduces FLOPs by approximately **44%** (194.11 G vs. 108.32 G) and parameters by **28%** (45.81 M vs. 32.99 M). Despite this reduction in complexity, LGEST achieves a substantial accuracy improvement of **5.55%** over SyCNN. This demonstrates that LGEST’s sparse expert routing mechanism is significantly more efficient at capturing discriminative features than dense 3D convolutions.

Table 1
Classification results for the IndianPines dataset (10% training samples).

Class	SVM	2D CNN	3D CNN	HybridSN	SyCNN	ViT	Cross ViT	Deep ViT	CaiT	HiT	Morphformer	SS-TMNet	GSC-ViT	LGEST (ours)
1	0.00 ± 0.00	15.56 ± 21.20	0.00 ± 0.00	0.00 ± 0.00	73.79 ± 8.25	0.00 ± 0.00	0.00 ± 0.00	7.95 ± 16.48	2.73 ± 5.45	14.19 ± 16.39	42.62 ± 23.14	68.73 ± 11.55	63.30 ± 30.15	86.46 ± 9.72
2	36.47 ± 2.36	88.73 ± 1.52	64.04 ± 3.58	60.05 ± 21.33	84.13 ± 1.33	48.68 ± 5.89	60.89 ± 5.29	78.18 ± 4.71	75.02 ± 2.33	86.47 ± 5.69	90.83 ± 1.71	87.35 ± 4.47	92.47 ± 1.39	92.51 ± 0.87
3	0.00 ± 0.00	87.70 ± 1.61	66.25 ± 6.79	45.77 ± 28.93	85.64 ± 3.64	10.76 ± 5.95	26.65 ± 20.21	71.36 ± 9.57	70.62 ± 3.68	87.36 ± 2.90	87.99 ± 1.82	87.70 ± 2.20	88.78 ± 0.38	91.25 ± 1.44
4	0.00 ± 0.00	91.35 ± 5.33	14.33 ± 16.14	24.53 ± 33.52	91.30 ± 2.80	36.88 ± 16.35	61.66 ± 13.63	87.78 ± 5.11	86.50 ± 2.86	86.87 ± 10.28	91.78 ± 5.64	89.03 ± 5.24	91.98 ± 4.12	94.24 ± 2.88
5	0.23 ± 0.23	92.15 ± 1.98	83.09 ± 10.96	38.52 ± 31.57	88.75 ± 2.27	13.84 ± 11.51	56.83 ± 6.31	57.34 ± 13.77	49.31 ± 15.23	82.94 ± 11.04	91.53 ± 2.18	87.31 ± 1.96	94.13 ± 0.70	93.43 ± 1.98
6	66.95 ± 0.55	93.22 ± 1.32	85.85 ± 4.15	62.89 ± 16.27	90.52 ± 1.96	58.41 ± 5.82	73.54 ± 8.45	82.43 ± 2.75	73.46 ± 1.89	90.63 ± 2.20	92.38 ± 2.04	92.49 ± 1.26	94.14 ± 0.49	93.76 ± 1.22
7	0.00 ± 0.00	0.00 ± 0.00	0.00 ± 0.00	0.00 ± 0.00	0.00 ± 0.00	0.00 ± 0.00	0.00 ± 0.00	0.00 ± 0.00	0.00 ± 0.00	0.00 ± 0.00	19.05 ± 27.81	0.00 ± 0.00	12.97 ± 25.95	35.85 ± 34.95
8	87.92 ± 1.23	99.88 ± 0.18	99.15 ± 0.65	80.74 ± 20.82	98.24 ± 1.09	94.21 ± 2.36	95.82 ± 2.33	98.64 ± 0.82	97.45 ± 2.00	97.18 ± 0.93	99.06 ± 1.15	98.74 ± 0.76	99.20 ± 1.04	99.75 ± 0.84
9	0.00 ± 0.00	0.00 ± 0.00	0.00 ± 0.00	0.00 ± 0.00	0.00 ± 0.00	0.00 ± 0.00	0.00 ± 0.00	0.00 ± 0.00	0.00 ± 0.00	0.00 ± 0.00	0.00 ± 0.00	0.00 ± 0.00	0.00 ± 0.00	3.78 ± 4.84
10	0.00 ± 0.00	81.88 ± 1.92	69.05 ± 4.09	43.36 ± 36.17	79.72 ± 2.67	6.32 ± 6.37	46.57 ± 12.51	65.91 ± 9.35	52.40 ± 5.01	83.13 ± 1.95	86.36 ± 3.02	81.95 ± 1.98	86.98 ± 0.84	87.97 ± 2.15
11	57.36 ± 0.32	95.13 ± 0.76	77.73 ± 2.98	79.81 ± 10.05	90.99 ± 1.75	57.90 ± 1.64	69.06 ± 4.13	81.24 ± 5.03	79.35 ± 3.63	92.09 ± 2.18	94.79 ± 1.25	93.12 ± 2.50	96.25 ± 0.52	96.05 ± 0.56
12	0.00 ± 0.00	85.03 ± 1.84	58.62 ± 5.55	43.26 ± 29.51	85.02 ± 3.37	8.90 ± 8.82	37.54 ± 9.46	68.99 ± 8.99	69.29 ± 5.64	82.69 ± 7.88	86.36 ± 3.29	82.35 ± 5.53	86.41 ± 4.92	90.22 ± 1.58
13	0.00 ± 0.00	94.53 ± 3.96	44.36 ± 27.71	38.22 ± 37.50	90.08 ± 2.82	38.77 ± 33.09	43.71 ± 29.41	87.16 ± 7.86	85.00 ± 7.88	94.93 ± 2.27	90.39 ± 5.25	96.16 ± 3.04	95.33 ± 1.57	95.70 ± 1.69
14	82.83 ± 0.30	97.71 ± 0.83	92.18 ± 2.36	82.45 ± 8.16	93.68 ± 2.15	81.65 ± 2.80	87.17 ± 2.65	91.47 ± 1.70	89.82 ± 2.02	94.57 ± 2.27	97.27 ± 0.90	95.34 ± 0.75	98.46 ± 0.18	98.30 ± 0.50
15	0.00 ± 0.00	91.98 ± 3.20	58.58 ± 21.34	36.13 ± 29.56	86.99 ± 7.18	10.56 ± 19.73	68.63 ± 12.40	89.07 ± 5.16	74.28 ± 6.11	90.27 ± 3.91	93.23 ± 1.62	93.61 ± 1.62	95.48 ± 1.43	95.13 ± 1.74
16	44.68 ± 25.03	25.39 ± 24.13	0.00 ± 0.00	0.00 ± 0.00	58.16 ± 22.31	0.00 ± 0.00	4.70 ± 10.44	32.34 ± 26.41	0.00 ± 0.00	22.73 ± 24.47	35.77 ± 32.18	11.01 ± 15.62	24.92 ± 30.52	57.39 ± 23.02
AA(%)	28.03 ± 1.23	70.12 ± 1.74	48.94 ± 2.95	40.83 ± 15.94	73.13 ± 2.22	30.96 ± 3.01	44.38 ± 5.63	60.31 ± 2.71	55.53 ± 1.11	68.08 ± 3.27	73.37 ± 2.55	71.48 ± 1.86	75.34 ± 2.94	80.72 ± 3.00
OA(%)	50.81 ± 0.26	91.09 ± 0.50	74.38 ± 2.46	65.64 ± 15.21	88.14 ± 1.19	51.93 ± 1.53	64.88 ± 4.51	79.48 ± 3.48	75.76 ± 1.52	88.77 ± 2.01	91.71 ± 0.87	89.77 ± 1.96	93.03 ± 0.46	93.69 ± 0.44
Kappa(%)	40.10 ± 0.38	89.80 ± 0.56	70.13 ± 2.99	59.60 ± 18.41	86.45 ± 1.36	42.30 ± 2.27	58.80 ± 5.56	76.25 ± 4.09	71.87 ± 1.83	87.13 ± 2.35	90.52 ± 0.99	88.28 ± 2.27	92.03 ± 0.53	92.80 ± 0.50

Table 2
Classification results for the KSC dataset (10% training samples).

Class	2D CNN	3D CNN	HybridSN	SyCNN	ViT	Cross ViT	Deep ViT	CaiT	HiT	SSFTT	Morphformer	SS-TMNet	GSC-ViT	LGEST (ours)
1	86.06 ± 1.52	91.22 ± 2.83	92.73 ± 0.94	91.75 ± 0.98	55.30 ± 4.30	76.22 ± 2.71	78.72 ± 0.85	70.51 ± 5.77	93.72 ± 1.25	90.53 ± 6.93	90.61 ± 4.34	89.99 ± 7.37	95.00 ± 0.62	91.72 ± 1.61
2	57.62 ± 9.53	65.44 ± 11.37	49.31 ± 16.05	63.21 ± 8.43	0.00 ± 0.00	0.82 ± 2.08	1.45 ± 2.57	0.80 ± 1.61	22.61 ± 14.75	73.37 ± 13.53	72.10 ± 11.72	73.62 ± 4.14	67.53 ± 13.93	77.77 ± 4.23
3	51.43 ± 6.90	67.50 ± 15.67	77.63 ± 10.51	81.42 ± 7.37	0.00 ± 0.00	0.00 ± 0.00	0.00 ± 0.00	0.00 ± 0.00	73.18 ± 10.19	67.84 ± 24.07	71.44 ± 24.15	75.99 ± 7.31	70.91 ± 9.22	75.47 ± 5.66
4	41.69 ± 9.14	50.13 ± 9.48	51.99 ± 20.42	63.04 ± 12.31	29.10 ± 21.65	38.95 ± 17.36	50.43 ± 3.34	25.23 ± 20.85	31.94 ± 18.55	77.06 ± 13.31	74.65 ± 13.11	66.28 ± 11.48	60.58 ± 3.08	77.25 ± 5.77
5	64.78 ± 12.26	60.13 ± 11.54	37.63 ± 16.43	53.64 ± 12.49	5.60 ± 8.74	44.29 ± 24.05	53.83 ± 23.55	14.35 ± 16.74	89.49 ± 5.52	72.93 ± 14.29	67.16 ± 23.72	82.07 ± 7.40	71.87 ± 8.73	95.79 ± 2.45
6	53.46 ± 10.36	81.64 ± 5.69	75.99 ± 6.46	75.47 ± 9.69	0.00 ± 0.00	0.00 ± 0.00	3.21 ± 7.54	0.00 ± 0.00	87.78 ± 6.72	72.03 ± 27.06	77.59 ± 15.60	70.48 ± 17.80	72.81 ± 8.24	90.03 ± 7.67
7	48.23 ± 29.09	97.87 ± 1.90	96.20 ± 3.22	96.17 ± 4.83	0.00 ± 0.00	0.00 ± 0.00	0.00 ± 0.00	0.00 ± 0.00	95.98 ± 6.48	55.20 ± 40.80	84.43 ± 21.33	73.48 ± 37.24	47.84 ± 32.15	98.48 ± 3.53
8	75.55 ± 2.21	85.21 ± 5.48	89.12 ± 3.93	83.91 ± 3.50	26.83 ± 8.37	72.92 ± 9.64	64.29 ± 8.39	65.48 ± 19.10	89.32 ± 3.81	85.22 ± 8.23	85.95 ± 7.26	86.57 ± 6.56	72.47 ± 5.70	81.92 ± 5.15
9	87.42 ± 1.55	94.01 ± 3.61	95.25 ± 3.21	92.92 ± 2.49	39.88 ± 9.02	66.11 ± 1.41	62.46 ± 1.45	61.28 ± 3.73	95.07 ± 4.08	95.28 ± 3.05	94.30 ± 4.44	94.07 ± 2.36	85.60 ± 2.80	93.12 ± 3.23
10	93.27 ± 3.50	88.87 ± 5.00	84.44 ± 3.88	69.70 ± 4.08	56.11 ± 10.20	71.40 ± 3.41	69.05 ± 4.67	63.63 ± 13.22	80.12 ± 4.96	98.35 ± 3.08	96.57 ± 2.73	95.75 ± 5.61	98.57 ± 1.33	99.15 ± 1.54
11	99.46 ± 0.54	96.92 ± 3.86	90.53 ± 9.54	88.99 ± 3.27	37.71 ± 18.47	69.44 ± 10.09	77.88 ± 8.11	40.20 ± 24.47	99.96 ± 0.09	98.95 ± 1.33	99.68 ± 0.43	99.95 ± 0.11	100.00 ± 0.00	100.00 ± 0.00
12	93.08 ± 2.47	94.40 ± 2.65	82.86 ± 6.76	74.62 ± 4.86	79.40 ± 11.34	87.55 ± 3.06	89.14 ± 1.88	85.59 ± 7.37	71.93 ± 7.60	98.36 ± 1.34	96.77 ± 3.76	97.23 ± 2.48	97.52 ± 1.94	99.29 ± 1.03
13	100.00 ± 0.00	100.00 ± 0.00	100.00 ± 0.00	99.78 ± 0.42	97.87 ± 3.46	100.00 ± 0.00	100.00 ± 0.00	98.92 ± 1.48	95.58 ± 3.19	99.96 ± 0.07	100.00 ± 0.00	100.00 ± 0.00	100.00 ± 0.00	100.00 ± 0.00
AA(%)	71.62 ± 3.21	81.80 ± 3.10	78.01 ± 3.45	78.35 ± 2.97	35.96 ± 3.98	51.55 ± 2.59	52.81 ± 1.72	44.72 ± 5.53	79.54 ± 3.87	82.26 ± 7.14	84.02 ± 8.31	84.04 ± 5.89	79.33 ± 3.65	90.32 ± 1.89
OA(%)	83.26 ± 1.39	87.98 ± 2.26	86.11 ± 2.25	84.03 ± 1.78	55.23 ± 4.10	70.45 ± 1.89	71.16 ± 1.13	64.81 ± 5.81	85.91 ± 2.83	90.69 ± 3.95	90.83 ± 4.41	90.21 ± 2.94	87.91 ± 1.55	92.59 ± 1.44
Kappa(%)	81.25 ± 1.56	86.59 ± 2.53	84.48 ± 2.52	82.18 ± 2.01	48.67 ± 4.85	66.58 ± 2.15	67.40 ± 1.27	60.00 ± 6.77	84.20 ± 3.20	89.57 ± 4.47	89.73 ± 4.97	89.06 ± 3.30	86.51 ± 1.74	91.75 ± 1.60

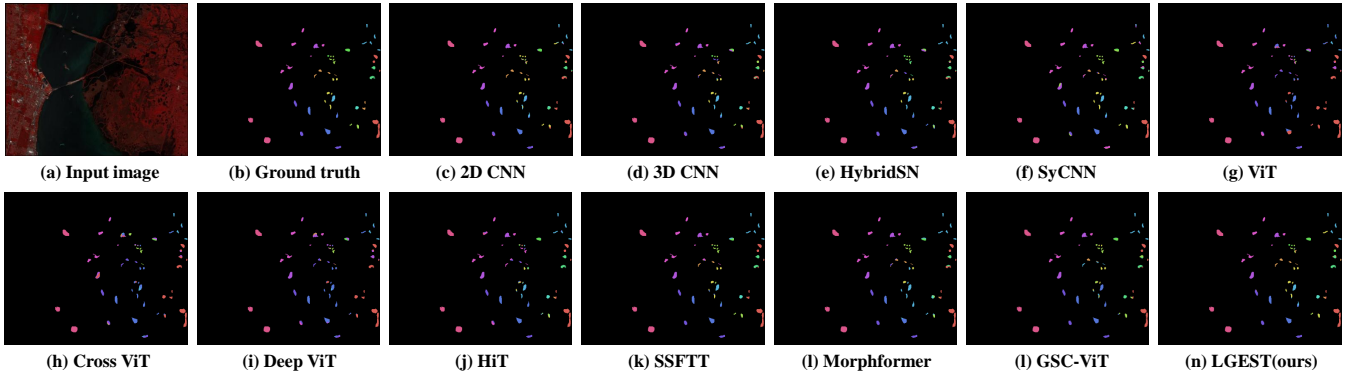


Fig. 4. Classification map of different methods on the KSC dataset (with 10% training samples).

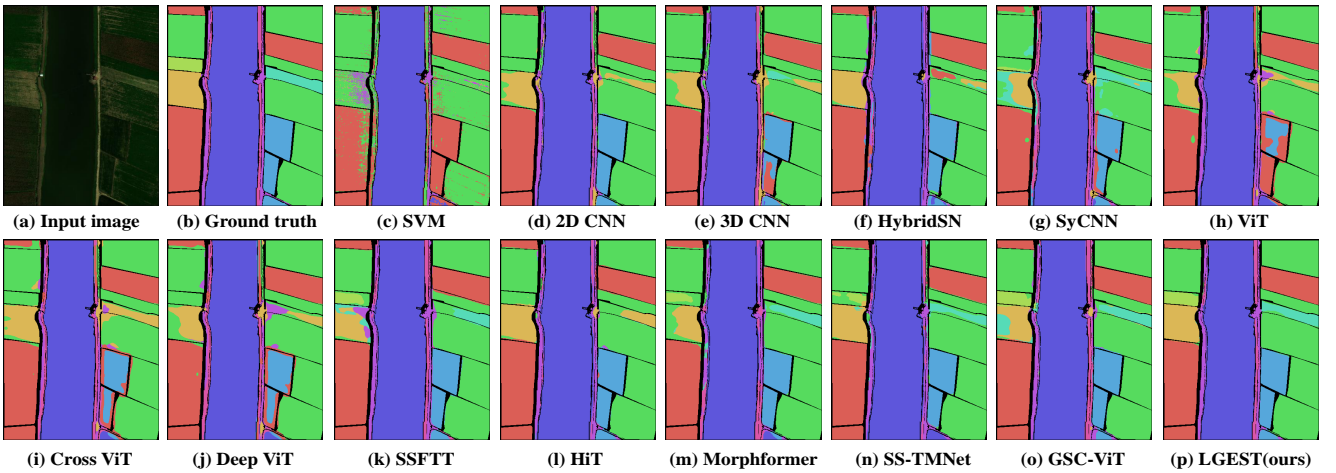


Fig. 5. Classification map of different methods on the WHU-Hi-LongKou dataset (with 0.1% training samples).

Effective Parameter Utilization: When compared to Transformer-based methods, LGEST exhibits a superior balance between model capacity and performance. While CaiT

possesses a massive parameter count (163.66 M), it fails to achieve competitive accuracy (75.76%), indicating severe redundancy. In contrast, LGEST utilizes a moderate

Table 3

Classification results for the Houston2013 dataset (10% training samples).

Class	SVM	3D CNN	HybridSN	SyCNN	ViT	Cross ViT	Deep ViT	CaiT	RvT	HiT	Morphformer	SS-TMNet	GSC-ViT	LGEST (ours)
1	90.94 ± 0.21	86.75 ± 1.72	83.54 ± 5.73	89.17 ± 1.11	79.78 ± 1.34	80.08 ± 2.46	86.50 ± 2.91	83.41 ± 3.72	88.36 ± 3.04	89.26 ± 1.68	92.63 ± 1.51	78.82 ± 24.36	91.79 ± 0.78	93.69 ± 1.94
2	96.56 ± 0.41	84.53 ± 3.22	83.45 ± 6.53	88.74 ± 2.34	63.64 ± 5.01	67.29 ± 5.82	76.70 ± 4.00	66.97 ± 4.18	89.50 ± 3.17	85.94 ± 2.11	93.44 ± 1.22	87.15 ± 10.45	93.66 ± 0.74	94.77 ± 1.18
3	59.63 ± 32.19	97.33 ± 1.59	93.32 ± 5.38	96.47 ± 1.60	95.24 ± 0.94	97.08 ± 1.46	97.51 ± 1.87	97.05 ± 0.82	97.50 ± 0.73	98.10 ± 1.03	98.48 ± 0.68	97.34 ± 1.56	98.16 ± 0.91	98.34 ± 1.34
4	93.87 ± 0.32	84.62 ± 3.48	78.82 ± 5.64	85.06 ± 2.97	64.98 ± 6.30	65.14 ± 7.32	76.68 ± 6.51	66.24 ± 5.60	84.97 ± 3.55	79.25 ± 4.31	93.93 ± 1.45	88.98 ± 7.77	94.24 ± 0.91	91.71 ± 1.62
5	90.97 ± 0.22	92.38 ± 3.09	91.79 ± 6.27	97.17 ± 1.08	87.35 ± 2.10	97.19 ± 1.05	98.47 ± 1.03	95.78 ± 0.89	99.44 ± 0.48	98.67 ± 0.64	99.21 ± 0.50	94.14 ± 10.30	99.83 ± 0.19	99.84 ± 0.15
6	89.94 ± 0.21	85.74 ± 1.15	85.82 ± 4.24	84.19 ± 2.62	79.63 ± 4.89	85.25 ± 1.34	83.03 ± 4.31	81.36 ± 3.86	84.47 ± 2.96	85.50 ± 0.89	90.48 ± 3.77	89.13 ± 3.97	88.23 ± 1.97	93.59 ± 1.34
7	68.20 ± 3.92	82.74 ± 2.43	74.68 ± 16.68	84.58 ± 1.64	76.11 ± 1.75	78.35 ± 2.83	79.15 ± 2.98	77.26 ± 2.75	85.91 ± 4.76	81.33 ± 3.59	94.29 ± 1.11	90.38 ± 4.78	94.54 ± 0.58	92.90 ± 1.90
8	54.07 ± 2.30	78.83 ± 3.65	81.37 ± 8.49	84.39 ± 2.27	68.37 ± 2.10	78.67 ± 4.86	84.78 ± 3.43	77.97 ± 3.09	93.39 ± 2.78	90.58 ± 2.67	94.79 ± 0.94	88.29 ± 12.62	95.05 ± 0.53	97.70 ± 0.52
9	62.16 ± 1.86	79.24 ± 4.63	48.18 ± 27.17	82.50 ± 0.98	68.85 ± 4.06	73.85 ± 5.29	81.16 ± 2.71	75.09 ± 2.26	85.93 ± 2.39	82.96 ± 1.88	91.72 ± 2.23	85.00 ± 9.28	93.16 ± 1.74	91.57 ± 1.31
10	38.44 ± 18.62	82.00 ± 4.61	83.08 ± 15.13	93.28 ± 2.40	72.94 ± 4.65	90.75 ± 2.31	90.18 ± 3.03	88.38 ± 1.23	91.26 ± 2.36	94.87 ± 1.68	97.93 ± 1.16	91.75 ± 11.30	98.01 ± 0.62	97.72 ± 1.42
11	63.58 ± 4.37	77.36 ± 7.39	66.87 ± 20.65	79.45 ± 3.59	64.59 ± 4.72	82.29 ± 4.34	84.94 ± 5.98	82.05 ± 3.33	90.80 ± 2.20	95.52 ± 1.85	98.15 ± 1.12	92.39 ± 11.71	96.88 ± 0.79	98.36 ± 0.92
12	36.27 ± 3.16	86.48 ± 2.90	84.45 ± 9.81	91.82 ± 2.34	66.68 ± 3.74	84.05 ± 2.35	89.57 ± 2.86	82.57 ± 3.85	89.46 ± 4.54	93.74 ± 2.43	95.42 ± 1.87	90.35 ± 12.27	96.60 ± 1.07	97.53 ± 0.63
13	0.00 ± 0.00	79.60 ± 4.81	63.93 ± 21.87	77.29 ± 4.65	29.73 ± 15.80	77.70 ± 6.18	86.16 ± 4.13	63.08 ± 9.59	83.28 ± 5.56	91.75 ± 2.48	93.17 ± 2.28	90.19 ± 6.77	92.41 ± 1.64	95.97 ± 1.05
14	85.30 ± 0.93	93.90 ± 3.94	81.82 ± 12.17	96.81 ± 1.51	82.64 ± 6.50	93.82 ± 3.86	95.27 ± 5.00	91.77 ± 4.29	99.04 ± 0.92	98.60 ± 0.84	98.84 ± 1.30	98.89 ± 2.15	98.45 ± 1.17	99.97 ± 0.05
15	98.52 ± 0.21	91.62 ± 2.43	75.10 ± 18.21	90.98 ± 4.09	75.32 ± 4.62	93.41 ± 2.50	94.59 ± 4.05	90.32 ± 5.29	95.91 ± 1.08	96.96 ± 1.30	97.53 ± 0.69	96.35 ± 1.65	97.30 ± 1.32	97.66 ± 1.65
AA(%)	70.49 ± 2.61	85.13 ± 1.23	80.25 ± 7.75	88.15 ± 0.52	71.27 ± 2.08	82.52 ± 1.81	86.24 ± 1.46	80.20 ± 1.97	91.08 ± 0.85	90.39 ± 1.23	94.92 ± 0.61	90.17 ± 8.45	94.74 ± 0.40	95.88 ± 0.40
OA(%)	71.83 ± 2.16	84.78 ± 1.29	79.49 ± 7.43	87.95 ± 0.67	72.30 ± 1.83	81.59 ± 1.89	86.07 ± 1.63	80.81 ± 1.46	90.42 ± 1.07	90.14 ± 1.51	95.34 ± 0.57	90.00 ± 9.45	95.44 ± 0.16	95.86 ± 0.58
Kappa(%)	69.47 ± 2.36	83.55 ± 1.39	77.85 ± 8.03	86.98 ± 0.72	70.01 ± 1.99	80.09 ± 2.05	84.93 ± 1.77	79.22 ± 1.59	89.65 ± 1.16	89.34 ± 1.63	94.96 ± 0.61	89.18 ± 10.22	95.07 ± 0.17	95.53 ± 0.63

Table 4

Classification results for the WHU-Hi-LongKou dataset (0.1% training samples).

Class	SVM	2D CNN	3D CNN	HybridSN	SyCNN	ViT	Cross ViT	Deep ViT	SSFTT	HiT	Morphformer	SS-TMNet	GSC-ViT	LGEST (ours)
1	74.34 ± 1.28	99.13 ± 0.31	95.12 ± 1.88	87.72 ± 22.49	97.26 ± 0.95	85.94 ± 3.12	89.96 ± 3.00	92.45 ± 2.62	98.31 ± 0.78	97.34 ± 2.65	98.36 ± 0.93	99.10 ± 0.51	99.20 ± 0.41	99.30 ± 0.27
2	27.18 ± 14.88	64.75 ± 7.57	59.79 ± 13.99	50.97 ± 28.43	83.74 ± 5.91	58.59 ± 3.23	64.29 ± 6.50	67.76 ± 7.26	75.38 ± 27.09	75.16 ± 9.31	87.14 ± 4.97	81.33 ± 3.20	84.17 ± 7.31	86.52 ± 3.67
3	0.00 ± 0.00	0.00 ± 0.00	0.00 ± 0.00	1.02 ± 2.82	3.11 ± 4.96	0.00 ± 0.00	0.00 ± 0.00	0.00 ± 0.00	2.39 ± 5.47	9.61 ± 17.94	26.74 ± 31.27	20.60 ± 31.25	48.96 ± 40.50	74.51 ± 24.81
4	85.37 ± 0.56	91.14 ± 2.13	88.82 ± 0.66	90.01 ± 5.91	93.53 ± 0.69	90.76 ± 0.48	92.13 ± 0.84	92.51 ± 0.91	94.44 ± 1.01	94.04 ± 1.77	94.45 ± 1.46	94.74 ± 1.13	96.88 ± 1.21	96.68 ± 0.98
5	0.00 ± 0.00	19.05 ± 21.20	44.35 ± 19.88	19.09 ± 27.35	57.19 ± 15.82	0.00 ± 0.01	7.92 ± 9.82	10.18 ± 8.02	37.26 ± 30.46	38.35 ± 14.23	57.82 ± 14.87	62.91 ± 18.67	60.47 ± 28.11	63.38 ± 16.32
6	1.86 ± 3.11	96.45 ± 1.71	92.14 ± 3.78	69.91 ± 35.94	92.14 ± 3.81	49.70 ± 28.56	71.19 ± 21.21	75.20 ± 18.12	96.02 ± 1.84	95.44 ± 2.54	96.77 ± 1.38	96.05 ± 1.96	95.46 ± 3.72	95.40 ± 1.78
7	99.64 ± 0.07	98.90 ± 0.53	99.08 ± 0.47	94.29 ± 2.36	98.77 ± 0.82	98.81 ± 0.35	99.32 ± 0.27	99.22 ± 0.25	97.58 ± 1.17	97.69 ± 0.64	98.73 ± 0.68	98.62 ± 0.70	99.58 ± 0.26	99.08 ± 0.50
8	53.22 ± 7.06	70.66 ± 7.33	49.20 ± 6.09	36.02 ± 21.45	62.39 ± 9.75	67.08 ± 3.58	67.19 ± 4.54	61.26 ± 10.73	57.93 ± 13.55	76.45 ± 3.72	66.03 ± 11.18	74.95 ± 4.38	70.39 ± 5.14	77.07 ± 4.79
9	0.00 ± 0.00	21.95 ± 19.93	28.23 ± 26.99	15.00 ± 19.24	58.03 ± 19.14	17.53 ± 16.93	47.72 ± 13.87	49.91 ± 14.56	23.32 ± 20.92	44.58 ± 13.62	45.97 ± 23.69	54.39 ± 15.41	63.83 ± 16.97	70.91 ± 6.76
AA(%)	40.14 ± 1.51	61.31 ± 3.86	58.46 ± 3.06	51.50 ± 12.80	70.04 ± 3.49	52.62 ± 6.09	59.46 ± 3.77	60.35 ± 3.58	64.30 ± 5.21	67.69 ± 4.28	71.81 ± 5.39	73.23 ± 4.31	78.90 ± 6.60	82.14 ± 3.19
OA(%)	79.98 ± 0.48	91.17 ± 1.11	89.40 ± 0.79	85.58 ± 7.17	92.40 ± 0.70	86.12 ± 1.43	88.61 ± 1.54	89.15 ± 1.31	91.92 ± 1.50	92.28 ± 1.66	93.54 ± 1.21	93.78 ± 0.76	95.01 ± 0.98	95.40 ± 0.50
Kappa(%)	72.76 ± 0.62	88.12 ± 1.57	85.64 ± 1.09	80.15 ± 10.49	89.88 ± 0.96	81.31 ± 1.98	84.76 ± 2.11	85.51 ± 1.80	89.16 ± 2.06	89.69 ± 2.24	91.37 ± 1.66	91.71 ± 1.05	93.40 ± 1.31	93.91 ± 0.66

Table 5

Complexity analysis on the Indian Pines dataset.

Methods	F(G)	P(M)	OA(%)↑
RvT	21.11	8.94	90.14 ± 0.90
CaiT	16.79	163.66	75.76 ± 1.52
SyCNN	194.11	45.81	88.14 ± 1.19
LGEST	108.32	32.99	93.69 ± 0.44

parameter scale (32.99 M) to achieve state-of-the-art performance (**93.69%**). Although the lightweight RvT incurs lower FLOPs, its limited capacity creates a performance bottleneck at roughly 90% OA. LGEST invests necessary computational resources to model complex local-global interactions, successfully breaking this bottleneck and offering the optimal trade-off for high-precision HSI classification tasks.

4.4. Ablation studies

4.4.1. Analysis of LGEST

In this section, we discuss the key components of LGEST and evaluate the functionality and effectiveness of its various modules using OA, AA, and κ metrics. We conducted detailed experiments on the Deep Spatial-Spectral Auto-Encoder (DSAE), the Cross-Interactive Mixed Expert Feature Pyramid (CIEM-FPN), and the Local-Global Expert System(LGES), and the experimental results are presented in Table 6.

Table 6

Ablation studies on key components of LGEST.

Methods	OA(%)↑	AA(%)↑	Kappa(%)↑
DSAE	91.50	74.49	90.30
DSAE w/Local Expert Group	93.05	77.25	92.05
LGEST	93.67	79.54	92.76
w/o CIEM-FPN	92.82	72.54	91.78
w/o Local Expert Group	93.28	77.31	92.31
w/o Global Expert Group	93.33	78.60	92.37
w/o Local-Global Expert System	92.87	76.55	91.86

Table 6 shows the poorest model results were from DSAE alone due to its lack of global spatial-spectral extraction capability. However, after adding the Local Expert Group (LEG), the overall accuracy (OA) significantly improved. For the Local Global Expert System (LGEST), the inclusion of CIEM-FPN, with its dual-branch Cross-Interactive module for global spatial-spectral feature fusion, had a significant impact on the average accuracy (AA) value. The AA decreased after removing the local-global expert system. To explore the impact of the local and global expert groups, separate tests were conducted, with similar results, demonstrating their comparable importance. Visualized t-SNE experiments were conducted to demonstrate the effect of different components on classification performance. The results (as shown in Fig. 8) show that the complete LGEST model significantly outperforms the removal of any individual module in terms of feature clustering.

4.4.2. Ablation study of the number of experts

This experiment explored the effect of changing the number of experts on four datasets. The number of experts affects the model’s ability to process complex data, but adding more experts doesn’t always improve performance. If there are too many experts, the model has a lot of parameters, which can cause expert competition. This happens when multiple experts work on similar data, which can result in each expert not getting enough training. On the other hand, if there are too few experts, each expert has to work on very different types of data, which can also hurt performance. Table 7 shows that the optimal number of experts varies for each dataset. Overall, the model performs best when there are four experts.

4.4.3. Ablation study of image patch size

The patch size in LGEST critically influences the balance between local detail preservation and global context capture, with optimal sizes varying according to the spatial characteristics of each dataset and the hierarchical architecture of the

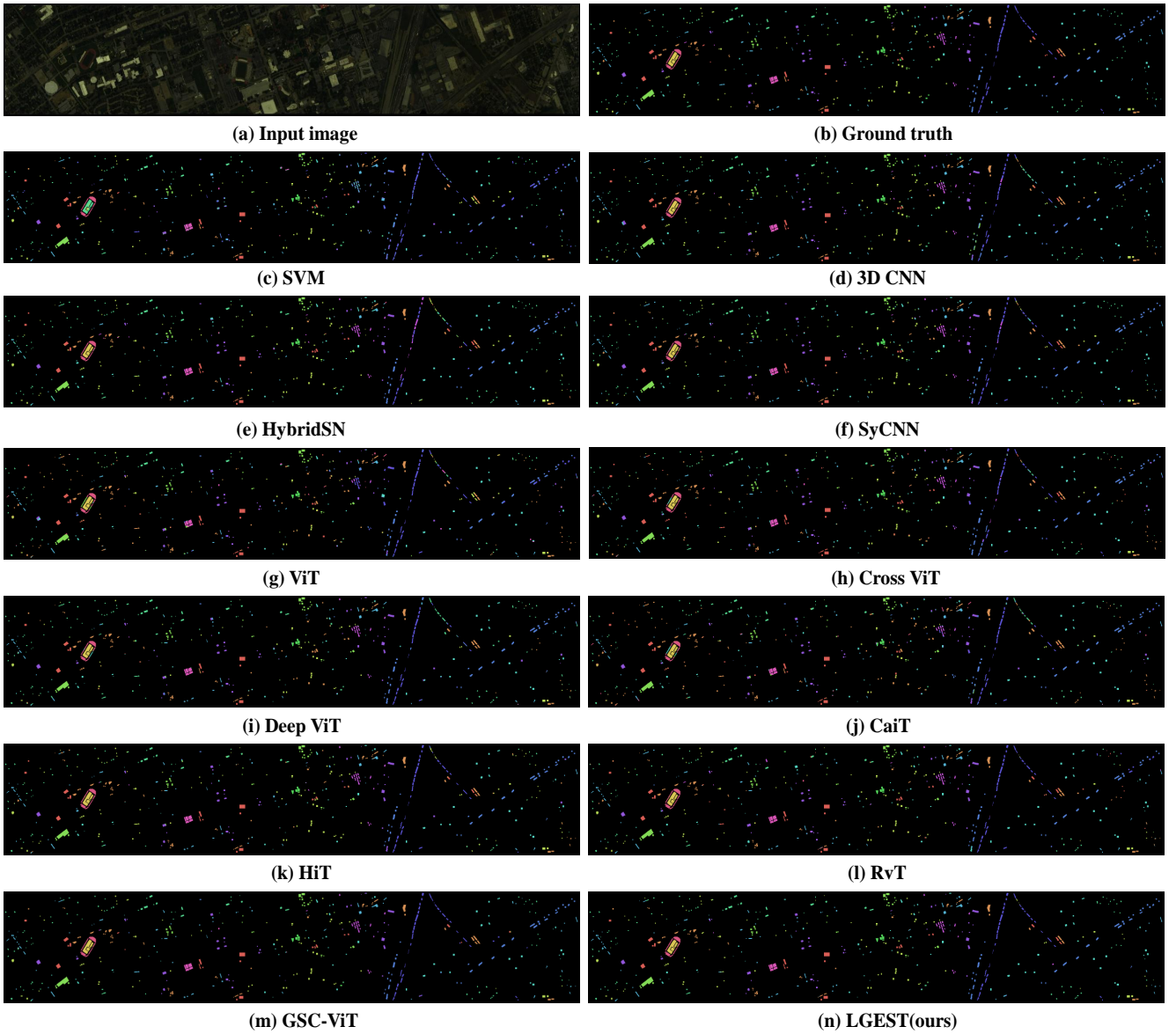


Fig. 6. Classification map of different methods on the Houston2013 dataset (with 10% training samples).

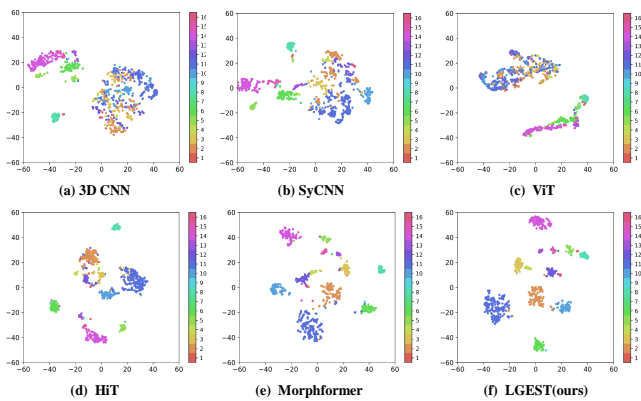


Fig. 7. Visualization of t-SNE data analysis on the IndianPines dataset.

model. As shown in Table 8, this variation demonstrates how the model adapts to different spatial configurations through its dual architecture: DSAE effectively compresses input patches while multi-scale fusion in CIEM-FPN and expert routing in LGES dynamically balance local and global in-

formation. This ablation study validates the robustness of LGEST across varying patch sizes, demonstrating its adaptive capacity to handle diverse spatial configurations through its hierarchical expert system.

4.4.4. Ablation study of the percentage of training samples

In this section, we conduct ablation experiments to analyze the effect of training sample percentages on the four datasets. The experimental results of the proposed LGEST are shown in Fig. 9. The results indicate that the overall OA value increases as the number of training samples rises. This trend is particularly prominent in the KSC dataset, where the OA value approaches 100% when the training samples reach 50%. Notably, the AA metrics for the Indian Pines dataset show a sharp decline as the training samples increase to 60%. We speculate that the increase in larger class samples negatively affects the classification accuracy of smaller classes. Overall, increasing the amount of data enables LGEST to capture more hyperspectral features.

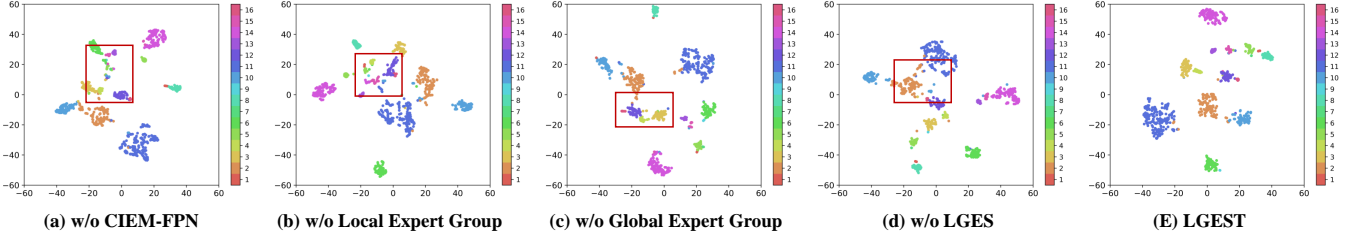


Fig. 8. Visualization of t-SNE data analysis on different modules in LGEST. The area marked by the red box is the confusing part.

Table 7
Ablation study on the number of experts. (best results in bold)

Datasets	Number	F(G)	P(M)	OA(%) \uparrow	AA(%) \uparrow	Kappa(%) \uparrow
Indian Pines	[2,2]	107.26	22.36	93.41 \pm 0.61	80.48 \pm 2.41	92.47 \pm 0.70
	[4,4]	108.32	32.99	93.69\pm0.44	80.72 \pm 3.00	92.80\pm0.50
	[8,8]	110.45	54.24	93.56 \pm 1.11	80.78\pm4.13	92.63 \pm 0.45
	[16,16]	114.70	96.75	93.45 \pm 0.47	79.53 \pm 3.49	92.51 \pm 0.54
KSC	[2,2]	106.77	20.58	92.59\pm1.44	90.32\pm1.89	91.75\pm1.60
	[4,4]	107.66	29.43	91.44 \pm 1.21	88.63 \pm 1.66	90.46 \pm 1.34
	[8,8]	109.43	47.14	91.24 \pm 2.12	88.05 \pm 3.22	90.24 \pm 2.36
	[16,16]	112.97	82.56	90.86 \pm 1.25	87.28 \pm 1.91	89.82 \pm 1.40
Houston2013	[2,2]	106.47	21.74	95.58 \pm 0.44	95.67 \pm 0.52	95.22 \pm 0.48
	[4,4]	107.48	31.78	95.86\pm0.58	95.88\pm0.40	95.53\pm0.63
	[8,8]	109.49	51.85	95.51 \pm 0.41	95.43 \pm 0.53	95.14 \pm 0.44
	[16,16]	113.50	92.00	95.77 \pm 0.49	95.67 \pm 0.62	95.42 \pm 0.53
WHU-Hi-LongKou	[2,2]	107.75	18.27	94.55 \pm 1.02	79.16 \pm 5.78	92.78 \pm 1.37
	[4,4]	108.40	24.76	95.17 \pm 0.87	81.55 \pm 3.84	93.61 \pm 1.16
	[8,8]	109.70	37.75	95.40\pm0.50	82.14\pm3.19	93.91\pm0.66
	[16,16]	112.30	63.73	94.44 \pm 1.10	77.75 \pm 4.70	92.62 \pm 1.50

Table 8
Ablation study on the patch sizes (best results in bold)

Datasets	Patch Size	OA(%) \uparrow	AA(%) \uparrow	Kappa(%) \uparrow
Indian Pines	9 \times 9	95.07 \pm 0.74	86.86\pm0.77	94.37 \pm 0.85
	11\times11	95.50\pm0.32	83.07 \pm 0.96	94.87\pm0.36
	13 \times 13	95.01 \pm 0.65	84.55 \pm 2.80	94.30 \pm 0.74
	15 \times 15	93.56 \pm 1.11	80.78 \pm 4.13	92.63 \pm 0.45
	17 \times 17	91.69 \pm 0.72	75.48 \pm 1.44	90.51 \pm 0.82
KSC	9 \times 9	89.21 \pm 1.21	83.28 \pm 1.72	87.97 \pm 1.35
	11 \times 11	90.27 \pm 0.96	84.10 \pm 2.15	89.14 \pm 1.07
	13 \times 13	93.34 \pm 0.53	90.09 \pm 0.49	92.58 \pm 0.60
	15 \times 15	91.24 \pm 2.12	88.05 \pm 3.22	90.24 \pm 2.36
	17\times17	93.36\pm1.33	91.17\pm2.79	92.60\pm1.49
Houston2013	9\times9	97.77\pm0.21	97.59\pm0.34	97.59\pm0.23
	11 \times 11	97.56 \pm 0.40	97.38 \pm 0.59	97.36 \pm 0.43
	13 \times 13	97.15 \pm 0.22	96.78 \pm 0.46	96.92 \pm 0.24
	15 \times 15	95.51 \pm 0.41	95.43 \pm 0.53	95.14 \pm 0.44
	17 \times 17	94.84 \pm 0.51	94.79 \pm 0.61	94.43 \pm 0.55
WHU-Hi-LongKou	9 \times 9	93.84 \pm 0.80	74.64 \pm 5.13	91.81 \pm 1.08
	11 \times 11	93.29 \pm 0.76	72.84 \pm 2.86	91.09 \pm 0.99
	13 \times 13	94.74 \pm 0.52	78.79 \pm 2.00	93.05 \pm 0.70
	15\times15	95.40\pm0.50	82.14\pm3.19	93.91\pm0.66
	17 \times 17	95.06 \pm 0.67	79.40 \pm 3.62	93.44 \pm 0.91

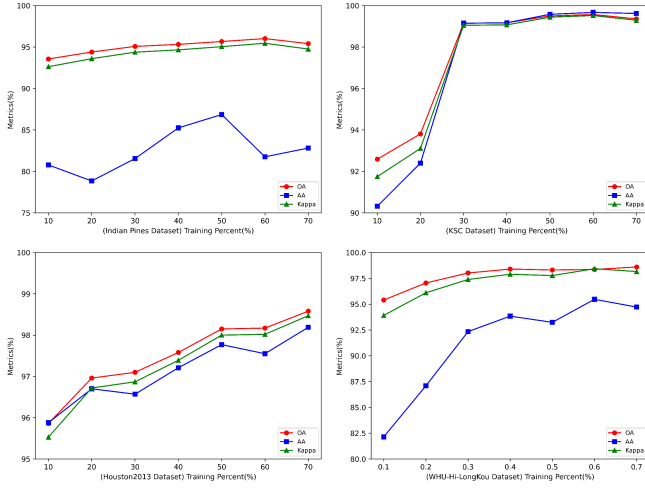


Fig. 9. Ablation study with training percentages on four datasets.

5. Conclusion

This paper introduces the Local-Global Expert Spatial-Spectral Transformer (LGEST), a novel framework for hyperspectral image (HSI) classification that overcomes key limitations of existing approaches through three pivotal innovations. First, the Deep Spatial-Spectral Autoencoder (DSAE) hierarchically compresses three-dimensional HSI cubes into compact, discriminative embeddings while preserving neighborhood coherence, thereby mitigating information loss in high-dimensional spaces. Second, the Cross-Interactive Mixed Expert Feature Pyramid (CIEM-FPN) employs cross-attention mechanisms and residual mixture-of-experts layers to dynamically fuse multi-scale features by adaptively weighting spectral and spatial cues via learnable

gating. Third, the Local-Global Expert System (LGES) utilizes sparsely activated expert pairs—where convolutional sub-experts capture fine-grained textures and transformer sub-experts model long-range dependencies—combined with confidence-aware routing for adaptive processing. Extensive experiments on four benchmark datasets demonstrate that LGEST achieves superior overall accuracy, average accuracy, and κ coefficient compared to state-of-the-art CNN and Transformer methods.

Future work will address the computational complexity of LGEST by investigating lightweight Transformer architectures and more efficient mixture-of-experts mechanisms, such as dynamic expert pruning and parameter sharing strategies. Finally, exploring few-shot learning scenarios with LGEST remains a priority, leveraging its expert-based architecture to improve generalization with limited labeled samples and thereby broadening its applicability to real-world remote sensing applications.

Data availability

Data will be made available on request.

Declaration of competing interest

The authors declare that they have no known competing financial interests or personal relationships that could have appeared to influence the work reported in this paper.

Funding

This work was jointly supported by the following projects: National Natural Science Foundation of China (NSFC) Fund under Grant 62301174 and 62403155. National Key Research and Development Program of China Fund under Grant 2021YFB3901204 and 2024YFC3015605. Guangzhou basic and applied basic research topics under Grant 2024A04J2081 and 2024A04J3369.

References

- [1] J.-P. Ardouin, J. Lévesque, T. A. Rea, A demonstration of hyperspectral image exploitation for military applications, in: 2007 10th International Conference on Information Fusion, IEEE, 2007, pp. 1–8.
- [2] P. Singh, P. C. Pandey, G. P. Petropoulos, A. Pavlides, P. K. Srivastava, N. Koutsias, K. A. K. Deng, Y. Bao, Hyperspectral remote sensing in precision agriculture: Present status, challenges, and future trends, in: Hyperspectral remote sensing, Elsevier, 2020, pp. 121–146.
- [3] S. Peyghambari, Y. Zhang, Hyperspectral remote sensing in lithological mapping, mineral exploration, and environmental geology: an updated review, *Journal of Applied Remote Sensing* 15 (3) (2021) 031501–031501.
- [4] S. Li, H. Wu, D. Wan, J. Zhu, An effective feature selection method for hyperspectral image classification based on genetic algorithm and support vector machine, *Knowledge-Based Systems* 24 (1) (2011) 40–48.
- [5] Y. Chen, Z. Liu, Z. Chen, Ams: A hyperspectral image classification method based on svm and multimodal attention network, *Knowledge-Based Systems* 314 (2025) 113236.
- [6] L. Ma, M. M. Crawford, J. Tian, Local manifold learning-based k -nearest-neighbor for hyperspectral image classification, *IEEE Transactions on Geoscience and Remote Sensing* 48 (11) (2010) 4099–4109.
- [7] J. Li, J. M. Bioucas-Dias, A. Plaza, Semisupervised hyperspectral image classification using soft sparse multinomial logistic regression, *IEEE Geoscience and Remote Sensing Letters* 10 (2) (2012) 318–322.
- [8] X. Yang, Y. Ye, X. Li, R. Y. Lau, X. Zhang, X. Huang, Hyperspectral image classification with deep learning models, *IEEE Transactions on Geoscience and Remote Sensing* 56 (9) (2018) 5408–5423.
- [9] Y. Chen, H. Jiang, C. Li, X. Jia, P. Ghamisi, Deep feature extraction and classification of hyperspectral images based on convolutional neural networks, *IEEE transactions on geoscience and remote sensing* 54 (10) (2016) 6232–6251.
- [10] A. B. Hamida, A. Benoit, P. Lambert, C. B. Amar, 3-d deep learning approach for remote sensing image classification, *IEEE Transactions on geoscience and remote sensing* 56 (8) (2018) 4420–4434.
- [11] X. Yang, W. Cao, Y. Lu, Y. Zhou, Hyperspectral image transformer classification networks, *IEEE Transactions on Geoscience and Remote Sensing* 60 (2022) 1–15.
- [12] D. Hong, Z. Han, J. Yao, L. Gao, B. Zhang, A. Plaza, J. Chanussot, Spectralformer: Rethinking hyperspectral image classification with transformers, *IEEE Transactions on Geoscience and Remote Sensing* 60 (2022) 1–15. doi:10.1109/TGRS.2021.3130716.
- [13] Y. Li, Y. Luo, L. Zhang, Z. Wang, B. Du, Mambahsi: Spatial-spectral mamba for hyperspectral image classification, *IEEE Transactions on Geoscience and Remote Sensing* 62 (2024) 1–16.
- [14] W. Fedus, B. Zoph, N. Shazeer, Switch transformers: Scaling to trillion parameter models with simple and efficient sparsity, *Journal of Machine Learning Research* 23 (120) (2022) 1–39.
- [15] H. Gao, Y. Yang, S. Lei, C. Li, H. Zhou, X. Qu, Multi-branch fusion network for hyperspectral image classification, *Knowledge-Based Systems* 167 (2019) 11–25.
- [16] X. Yang, X. Zhang, Y. Ye, R. Y. Lau, S. Lu, X. Li, X. Huang, Synergistic 2d/3d convolutional neural network for hyperspectral image classification, *Remote Sensing* 12 (12) (2020) 2033.
- [17] S. K. Roy, G. Krishna, S. R. Dubey, B. B. Chaudhuri, Hybridsn: Exploring 3-d-2-d cnn feature hierarchy for hyperspectral image classification, *IEEE Geoscience and Remote Sensing Letters* 17 (2) (2019) 277–281.
- [18] B. Xi, J. Li, Y. Diao, Y. Li, Z. Li, Y. Huang, J. Chanussot, Dgssc: A deep generative spectral-spatial classifier for imbalanced hyperspectral imagery, *IEEE Transactions on Circuits and Systems for Video Technology* 33 (4) (2022) 1535–1548.
- [19] A. Dosovitskiy, L. Beyer, A. Kolesnikov, D. Weissenborn, X. Zhai, T. Unterthiner, M. Dehghani, M. Minderer, G. Heigold, S. Gelly, J. Uszkoreit, N. Houlsby, An image is worth 16x16 words: Transformers for image recognition at scale, in: International Conference on Learning Representations, 2021, pp. 1–16.
- [20] D. Zhou, B. Kang, X. Jin, L. Yang, X. Lian, Z. Jiang, Q. Hou, J. Feng, Deepvit: Towards deeper vision transformer, arXiv preprint arXiv:2103.11886 (2021).
- [21] X. Yang, W. Cao, Y. Lu, Y. Zhou, Qtn: Quaternion transformer network for hyperspectral image classification, *IEEE Transactions on Circuits and Systems for Video Technology* 33 (12) (2023) 7370–7384.
- [22] X. Huang, Y. Zhou, X. Yang, X. Zhu, K. Wang, Ss-tmnet: Spatial-spectral transformer network with multi-scale convolution for hyperspectral image classification, *Remote Sensing* 15 (5) (2023) 1206.
- [23] Z. Zhao, X. Xu, S. Li, A. Plaza, Hyperspectral image classification using groupwise separable convolutional vision transformer network, *IEEE Transactions on Geoscience and Remote Sensing* 62 (2024) 1–17.

- [24] J. Wang, X. Tan, Mutually beneficial transformer for multimodal data fusion, *IEEE Transactions on Circuits and Systems for Video Technology* 33 (12) (2023) 7466–7479. doi:10.1109/TCSVT.2023.3274545.
- [25] L. Sun, G. Zhao, Y. Zheng, Z. Wu, Spectral–spatial feature tokenization transformer for hyperspectral image classification, *IEEE Transactions on Geoscience and Remote Sensing* 60 (2022) 1–14.
- [26] L. Song, Z. Feng, S. Yang, X. Zhang, L. Jiao, Interactive spectral-spatial transformer for hyperspectral image classification, *IEEE Transactions on Circuits and Systems for Video Technology* (2024).
- [27] C. Jia, X. Zhang, H. Meng, S. Xia, L. Jiao, Centerformer: A center spatial-spectral attention transformer network for hyperspectral image classification, *IEEE Journal of Selected Topics in Applied Earth Observations and Remote Sensing* (2025) 1–18 doi:10.1109/JSTARS.2025.3529985.
- [28] X. Zhang, Y. Su, L. Gao, L. Bruzzone, X. Gu, Q. Tian, A lightweight transformer network for hyperspectral image classification, *IEEE Transactions on Geoscience and Remote Sensing* 61 (2023) 1–17. doi:10.1109/TGRS.2023.3297858.
- [29] Y. Zhang, W. Li, W. Jia, M. Zhang, R. Tao, S. Liang, Cross-domain hyperspectral image classification based on bi-directional domain adaptation, *IEEE Transactions on Circuits and Systems for Video Technology* (2025) 1–1 doi:10.1109/TCSVT.2025.3586282.
- [30] Y. Feng, J. Zhu, R. Song, X. Wang, S2eft: Spectral-spatial-elevation fusion transformer for hyperspectral image and lidar classification, *Knowledge-Based Systems* 283 (2024) 111190.
- [31] Y. He, B. Tu, B. Liu, J. Li, A. Plaza, 3dss-mamba: 3d-spectral-spatial mamba for hyperspectral image classification, *IEEE Transactions on Geoscience and Remote Sensing* (2024).
- [32] M. Cao, W. Xie, X. Zhang, J. Zhang, K. Jiang, J. Lei, Y. Li, M3amba: Clip-driven mamba model for multimodal remote sensing classification, *IEEE Transactions on Circuits and Systems for Video Technology* (2025) 1–1 doi:10.1109/TCSVT.2025.3549750.
- [33] Y. Li, D. Li, W. Xie, J. Ma, S. He, L. Fang, Semimamba: Mamba-driven semi-supervised multimodal remote sensing feature classification, *IEEE Transactions on Circuits and Systems for Video Technology* (2025) 1–1 doi:10.1109/TCSVT.2025.3560615.
- [34] J. Sheng, J. Zhou, J. Wang, P. Ye, J. Fan, Dualmamba: A lightweight spectral-spatial mamba-convolution network for hyperspectral image classification, *IEEE Transactions on Geoscience and Remote Sensing* (2024).
- [35] H. Cao, Y. Guo, Y. Chu, Y. Wang, J. Duan, P. Li, Few-shot hyperspectral image classification with mamba and manifold convolution fusion network, *Knowledge-Based Systems* (2025) 114531.
- [36] Z. Pan, C. Li, A. Plaza, J. Chanussot, D. Hong, Hyperspectral image classification with mamba, *IEEE Transactions on Geoscience and Remote Sensing* (2024).
- [37] H. Zhang, H. Liu, Z. Shi, S. Mao, N. Chen, Conv-mamba: Combining mamba with cnn for hyperspectral image classification, *Neurocomputing* (2025) 131016.
- [38] Y. He, B. Tu, P. Jiang, B. Liu, J. Li, A. Plaza, Igroupss-mamba: Interval group spatial-spectral mamba for hyperspectral image classification, *IEEE Transactions on Geoscience and Remote Sensing* (2024).
- [39] A. Yang, M. Li, Y. Ding, L. Fang, Y. Cai, Y. He, Graphmamba: An efficient graph structure learning vision mamba for hyperspectral image classification, *IEEE Transactions on Geoscience and Remote Sensing* (2024).
- [40] T.-Y. Lin, P. Dollár, R. Girshick, K. He, B. Hariharan, S. Belongie, Feature pyramid networks for object detection, in: *Proceedings of the IEEE conference on computer vision and pattern recognition*, 2017, pp. 2117–2125.
- [41] C.-F. R. Chen, Q. Fan, R. Panda, Crossvit: Cross-attention multi-scale vision transformer for image classification, in: *Proceedings of the IEEE/CVF international conference on computer vision*, 2021, pp. 357–366.
- [42] J. L. Ba, J. R. Kiros, G. E. Hinton, Layer normalization, *ArXiv e-prints* (2016) arXiv-1607.
- [43] R. Hou, H. Chang, B. Ma, S. Shan, X. Chen, Cross attention network for few-shot classification, *Advances in neural information processing systems* 32 (2019).
- [44] H. Touvron, M. Cord, A. Sablayrolles, G. Synnaeve, H. Jégou, Going deeper with image transformers, in: *Proceedings of the IEEE/CVF international conference on computer vision*, 2021, pp. 32–42.
- [45] S. K. Roy, A. Deria, C. Shah, J. M. Haut, Q. Du, A. Plaza, Spectral–spatial morphological attention transformer for hyperspectral image classification, *IEEE Transactions on Geoscience and Remote Sensing* 61 (2023) 1–15.